ACOUSTICS

Acoustic metamaterials: From local resonances to broad horizons

Guancong Ma* and Ping Sheng*

Within a time span of 15 years, acoustic metamaterials have emerged from academic curiosity to become an active field driven by scientific discoveries and diverse application potentials. This review traces the development of acoustic metamaterials from the initial findings of mass density and bulk modulus frequency dispersions in locally resonant structures to the diverse functionalities afforded by the perspective of negative constitutive parameter values, and their implications for acoustic wave behaviors. We survey the more recent developments, which include compact phase manipulation structures, superabsorption, and actively controllable metamaterials as well as the new directions on acoustic wave transport in moving fluid, elastic, and mechanical metamaterials, graphene-inspired metamaterials, and structures whose characteristics are best delineated by non-Hermitian Hamiltonians. Many of the novel acoustic metamaterial structures have transcended the original definition of metamaterials as arising from the collective manifestations of constituent resonating units, but they continue to extend wave manipulation functionalities beyond those found in nature.

INTRODUCTION

The study of electromagnetic and acoustic waves is an endeavor that dates back centuries. Starting about three decades ago, the incipient stage of a revolution has occurred in this classic field, propelled by both theory and experiments, which demonstrated the feasibility of realizing man-made materials with wave manipulation functionalities beyond the defined limits of those found in nature. Initially inspired by an analogy with the quantum mechanical band theory of solids in which electronic waves interact with a periodically arranged atomic lattice to form energy bands separated by bandgaps, photonic and phononic crystals were proposed theoretically (1–4) and realized experimentally (5–7). To be effective, the lattice constants of photonic and phononic crystals have to be on the order of the relevant electromagnetic and elastic/acoustic wavelength. Owing to the large wavelength of acoustic waves in the audible regime ranging from centimeters to meters, phononic crystals were mostly realized in the ultrasonic regime, because lower frequencies would require rather bulky samples (6). The emergence of acoustic metamaterials not only resolved the sample size problem but also introduced new functionalities not found previously.

The term "metamaterials" was originally coined to denote a class of structured composites whose wave functionalities arise as the collective manifestations of its locally resonant constituent units. Because the resonant frequency of a unit depends only on its inertia (for example, the mass) and the restoring force (for example, that of the spring), the relevant wavelength at the resonant frequency can be orders of magnitude larger than the physical dimension of the resonant unit. This subwavelength characteristic is therefore a common feature of all types of metamaterials, whose definition has now broadened to include subwavelength structures with functionalities not found in nature. This review would consider the term "metamaterials" in such a broader sense.

Acoustic metamaterials are useful in manipulating acoustic waves that are governed by Newton's law of motion, the fluid continuity equation, and the thermodynamic equation of state (for adiabatic process). The acoustic wave equation in a homogeneous medium absent of a source is given by

$$\nabla^2 P - \frac{\rho}{\kappa}\frac{\partial^2 P}{\partial t^2} = 0$$

where P is pressure and the two constitutive parameters are the mass density ρ and the bulk modulus κ. The speed of sound v is given by $\sqrt{\kappa/\rho}$. In an acoustic metamaterial, the two constitutive parameters can take unusual values when considered in the effective medium sense (for example, negative, zero, or close to divergent). Such values imply acoustic wave characteristics that are usually not associated with ordinary composites. However, if such unusual features arise from local resonances of the constituent components, then they are "narrow band" in character (that is, occurring only in the vicinities of the resonant frequencies).

Acoustic waves in fluids are longitudinal scalar waves. In contrast, electromagnetic waves are transverse vector waves with two polarizations. However, an analogy between the two can still be made easily, owing to their wave equations having the same mathematical form. The two constitutive parameters can be mapped as $\rho \rightarrow \epsilon$ and $\kappa \rightarrow \mu^{-1}$, where ϵ and μ are dielectric constant and magnetic permeability, respectively. This also indicates that the two types of waves share much (but not all) of the underlying physics, which is the reason that electromagnetic/optical metamaterials and the related intriguing phenomena [such as negative refraction (8, 9), superlensing (10), and cloaking (11, 12)] have developed hand in hand with their counterparts in acoustic metamaterials.

In what follows, we first delineate the local resonant structures that give rise to the unusual values of effective mass density and bulk modulus. Decorated membrane resonators (DMRs) are a special class of metamaterials that were chosen to demonstrate the unusual values of effective mass density and bulk modulus dispersions and their underlying physics. The diverse functionalities of acoustic metamaterials will then be explored, including superresolution, cloaking, phase manipulation using space-coiling structures, absorption, and

Department of Physics and Institute for Advanced Study, Hong Kong University of Science and Technology, Clear Water Bay, Kowloon, Hong Kong, China.
*Corresponding author. E-mail: phmgc@ust.hk (G.M.); sheng@ust.hk (P.S.)

actively controllable structures. Emerging directions, such as moving media, nonlinearity, and graphene-inspired acoustic composites, are surveyed.

SPRING-MASS MODEL AND DYNAMIC EFFECTIVE MASS

A composite that allows relative motions between the constituent components can display an inertial response that differs from that of a rigid body. A familiar example is the sloshing of water inside a bucket, which makes it difficult to carry. To mathematically clarify this effect, we consider the dynamics of a simple one-dimensional coupled oscillator under an external harmonic excitation force $F(\omega)$, where ω is the angular frequency. An illustration of this model is shown in Fig. 1A. If mass M_2 is considered to slide inside the cavity formed by mass M_1 without friction, then the total force exerted on M_1 is given by $F(\omega) + K(x_2 - x_1)$, where the second term arises from the contact point where the spring is fixed on mass M_1, and x_1 and x_2 are the displacements of M_1 and M_2, respectively. Mass M_2 can undergo harmonic oscillation, whose equation of motion is given by $M_2\ddot{x}_2 = -K(x_2 - x_1)$, where the double overdot denotes a second-order time derivative. By equating $\ddot{x}_{(1,2)}$ with $-\omega^2 x_{1,2}$, one can solve x_2 in terms of x_1 so that, in terms of the displacement x_1, we have

$$F = \left(M_1 + \frac{K}{\omega_0^2 - \omega^2}\right)\ddot{x}_1$$

where $\omega_0 = \sqrt{K/M_2}$ is the local resonance frequency of M_2. If an observer cannot see the inner structure of this system, then the system's "apparent" inertia acquires a frequency dispersion

$$\overline{M}(\omega) = M_1 + \frac{K}{\omega_0^2 - \omega^2}$$

as plotted in Fig. 1B. The system's inertial response $\overline{M}(\omega)$ can deviate significantly from its static value. It is therefore reasonable to describe the system with a dynamic effective mass, which allows Newton's second law to be satisfied in a new form: $F = \overline{M}(\omega)\ddot{x}_1$. The above discussion suggests that when there are relative motions between the constituent components in a composite, then one should define a dynamic mass density $\bar{\rho}$ as

$$\bar{\rho} = \langle f \rangle / \langle \ddot{x} \rangle \tag{1}$$

where f is the force density, x is the sample (unit cell) displacement, and the angular brackets denote averaging over the surface area of the sample (or unit cell) under consideration.

More thorough treatments regarding the effective mass of similar spring-mass systems can be found in Milton and Willis (13) and Mei et al. (14). An experimental visualization can be found in Yao et al. (15).

Effective mass dispersion between two resonances

A very common and general situation in which mass density dispersion can also appear is the so-called antiresonance condition, which can occur at a frequency between two resonances. Consider the average displacement of a sample that has two resonances at frequencies

ω_1 and ω_2. When the external driving frequency ω is between the two, both modes will be excited, but with opposite phases. The average displacement can cross zero at a certain frequency, denoted as the antiresonance frequency $\tilde{\omega}$ (Fig. 1C). Because $\langle \ddot{x} \rangle = -\omega^2 \langle x \rangle$ for harmonic motion, it follows that, in accordance with Eq. 1, the dynamic mass density can display a frequency dispersion, as shown in Fig. 1B.

Composites that display such frequency-dispersive properties are fascinating for both fundamental and practical purposes. Initial realization is achieved by using an acoustic metamaterial incorporating local resonances. This metamaterial is a matrix of silicone-coated metallic spheres embedded in epoxy (16). Photographic images of a unit cell and a matrix are shown in Fig. 2A. The sample has low-frequency resonances that are characterized solely by the relative motions of constituents internal to the elementary building blocks. The lowest frequency resonance, at around 400 Hz, corresponds with the displacement of the metallic sphere. The second resonance, at around 1350 Hz, corresponds with the displacement of the silicone rubber layer, with the metallic sphere being nearly stationary. Together, they lead to a strong frequency dispersion in the dynamic mass density $\bar{\rho}$ (17), as described previously. In particular, when the effective dynamic mass density either diverges to a large value or exhibits a negative value, acoustic waves become strongly attenuated inside the composite structure, and near-total reflection of the wave occurs.

## EFFECTIVE BULK MODULUS AND SYMMETRY OF THE RESONANCES

Effective mass dispersion (in frequency) is always associated with the displacement of the system's center of mass. However, if the deformation involves compression-extensional motion, then it is entirely possible for the center of mass to be stationary. This is precisely what occurs in Helmholtz resonators, in which the effective bulk modulus, rather than the effective mass density, becomes frequency-dependent.

The resonance-induced anomalous effective bulk modulus $\bar{\kappa}$ was first demonstrated by Fang et al. (18) on ultrasound by a waveguide shunted by a chain of Helmholtz resonators. Helmholtz resonance is characterized by the oscillation of the fluid in the neck section under the restoring force provided by the compression and expansion of the fluid in the cavity. An illustration of the relevant sample is shown in Fig. 2B. The sample is subwavelength in its dimension. Negative bulk modulus, caused by the frequency dispersion of the local resonances, was observed.

The effective mass density and bulk modulus behaviors are associated with two distinct spatial symmetries of the relevant resonances. For simplicity, let us consider harmonic motions in one dimension, in which it can be easily shown that they can be considered as the weighted superposition of symmetric and antisymmetric motions (that is, the dipolar and monopolar resonant displacements, respectively). Li and Chan (19) first related acoustic responses to the symmetry of motions in the context of the Mie resonance of soft rubber spheres. They pointed out that modes with dipolar symmetry contribute to the inertial response, whereas modes with monopole symmetry generate a dominantly compressive/expansive motion, namely, a bulk modulus–type response. Later studies also showed that modes with higher angular momenta would have responses with interesting consequences for elastic waves (20, 21).
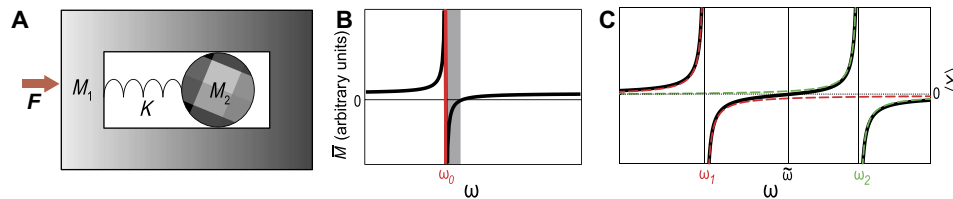
Fig. 1. The origin of anomalous constitutive parameters in acoustics. (**A**) A spring-coupled mass-in-mass oscillator. M_2 is assumed to slide without friction inside a cavity formed by M_1, and K is the spring constant. (**B**) The oscillator's apparent mass $\overline{M}$ plotted as a function of angular frequency ω, where $\omega_0 = \sqrt{K/M_2}$ is the resonant frequency. $\overline{M}$ is divergent at ω_0 and can take negative values in a narrow frequency region that is shaded gray. (**C**) If there are two resonances, the average displacement $\langle X \rangle$ can cross zero at an antiresonance frequency $\tilde{\omega}$, at which the effective mass/mass density displays a frequency dispersion similar to that shown in (B). Here, the red and green dashed curves show the displacement associated with the first and second resonances (denoted ω_1 and ω_2), respectively. The black solid curve represents the sum of the two displacements, and it crosses zero at $\tilde{\omega}$.
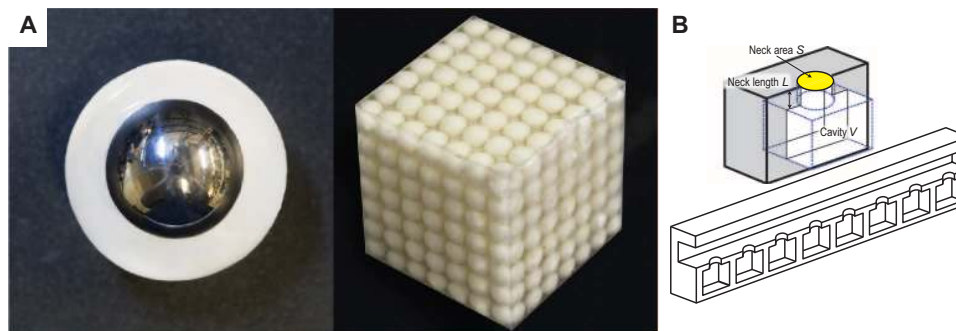
Fig. 2. Initial realizations of locally resonant acoustic metamaterials. (**A**) Images of the sample that first realized a local resonance–induced anomalous mass effect (*16*). Left: The cut-away view of a sample unit cell consisting of a small metallic sphere coated by a thin uniform layer of silicone rubber. Right: The sample made by using epoxy to glue together the units shown on the left. The effective frequencies for total reflection by the sample were shown to correspond to a wavelength that is between one and two orders of magnitude larger than the size of the lattice constant, which is 1.55 cm. (**B**) An illustration of the sample, comprising a series of Helmholtz resonators connected to one side of a conduit, that realized the frequency dispersion for the bulk modulus (*18*).

## Doubly negative mass density and bulk modulus

By overlapping the frequency responses with the two symmetry types, it is possible to realize acoustic double negativity. This is achievable through several approaches. First, a single resonator can have multiple eigenmodes exhibiting distinctive symmetries. By careful design, it is possible to tune the relative frequencies of these eigenmodes to enable the realization of simultaneously negative $\bar{\rho}$ and $\bar{\kappa}$ values. Examples include coupled membrane resonators (*22*). Mie resonances of porous silicone rubber spheres are also shown to exhibit a negative acoustic index (*23*). Alternatively, combining two different resonating structures, each having one type of symmetry, can also lead to double negativity. Some theoretical proposals can be found in Ding *et al.* (*24*), Christensen *et al.* (*25*), and Fok and Zhang (*26*). The first successful experimental demonstration of acoustic double negativity was accomplished by Lee *et al.* (*27–29*) in a series of publications. Frequency dispersion in $\bar{\rho}$ was induced in a sample comprising a waveguide segmented by elastic membranes (*27*). The same waveguide is simultaneously shunted by a series of side holes to give rise to a frequency dispersion in $\bar{\kappa}$ (*28*). Overlap in these two dispersive frequency ranges leads to double negativity (*29*). Recently, the interaction between eigenmodes with identical symmetry type also produced double negativity (*30*). This will be detailed in "Acoustic Superlens."

There exists a multitude of approaches for the retrieval of the effective constitutive parameters $\bar{\rho}$ and $\bar{\kappa}$ for locally resonant acoustic structures (*17, 31–35*). The underlying philosophy in targeting the re-

production of far-field scattering properties by a uniform medium characterized by the effective parameters, in which the complex structures of the elementary scattering units are "internalized" to appear as the frequency variations in $\bar{\rho}$ and $\bar{\kappa}$, is generally similar.

MEMBRANE-TYPE ACOUSTIC METAMATERIALS

DMRs constitute a class of acoustic metamaterials that can display both mass and bulk modulus frequency dispersions, as well as double negativity, over certain frequency ranges. Typically, its effective frequency regime falls within the audible range of 50 to 2000 Hz; hence, the application potentials are obvious because the membranes are thin and light. An example is shown in Fig. 3A. A flexible elastic membrane that is submillimeters thick and several centimeters wide is fixed on a rigid rim. A uniform prestress is applied to provide the proper restoring force for oscillations. A rigid platelet is attached to the center of the membrane, whose mass is set by the desired resonant frequencies. This structure may be modeled as a spring-mass oscillator by simply regarding the central platelet as the mass and the membrane as the spring (also with a small mass) (*36*). The response of a DMR to an incident acoustic wave is characterized by its normal displacement profile $W(\boldsymbol{x})$. Because of the membrane's small thickness, the DMR's low-frequency eigenmodes are dipolar in symmetry, as the compressive oscillations of the membrane are necessarily in the high-frequency
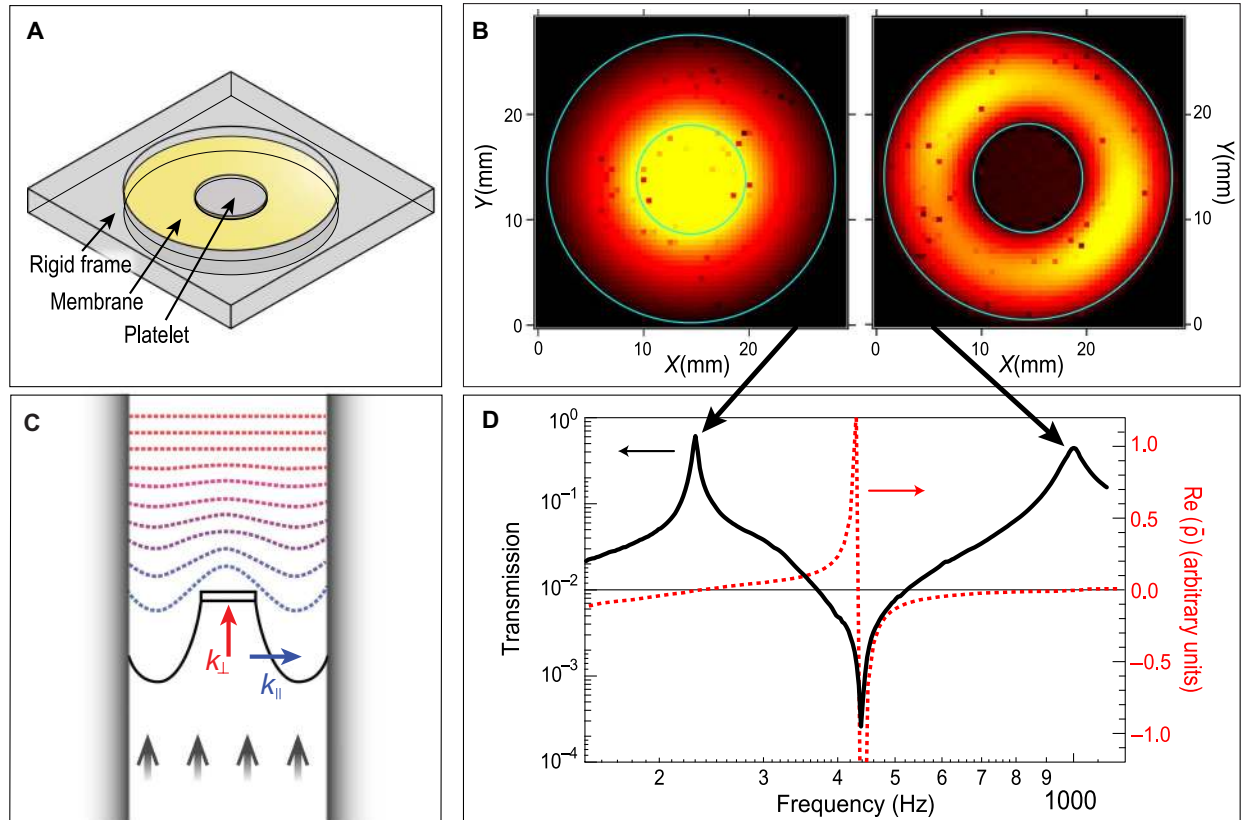
Fig. 3. Single membrane with negative effective mass density. (**A**) A schematic drawing of a typical DMR (*36*). (**B**) Out-of-plane displacement amplitude |$W(x)$| of the low-frequency eigenmodes (measured with a laser Doppler vibrometer) of two DMRs (*194*). Light yellow indicates a large normal displacement amplitude, whereas darker colors indicate small or no normal displacement. Cyan circles delineate the edge of the membrane and the position of the platelet. The first mode is characterized by the large up-and-down oscillation of the platelet, pulling along the entire structure (left). In the second mode, the platelet is almost motionless (right), and the oscillation amplitude is largest in the surrounding membrane. (**C**) A schematic illustration indicating that, as a result of the deep-subwavelength size of the DMR, the large in-plane wave vectors $k_\parallel$ only contribute to evanescent waves (blue dashed lines), owing to the fact that the lateral fast variations of the up-and-down displacements tend to cancel each other in air, and the net amplitude decays exponentially as a result. The far-field propagating wave is determined by the $k_\perp$ of the surface-averaged component of the normal displacement (red dashed lines). In the system shown here, the DMR (black) is blocking a one-dimensional waveguide, and a planar sound wave impinges from the bottom. The reflected field is not shown. (**D**) Measured amplitude transmission coefficient of a DMR (black solid curve, left axis) and the real part of the calculated effective mass density $\bar{\rho}$ (red dashed curve, right axis). Various features are explained in the text.

regime. Typically, two eigenmodes can be found below 1 kHz. Their normal displacement profiles are shown in Fig. 3B. The dipolar symmetry of the resonances implies that the scattering characteristics of the DMR can be reflected in the frequency variation of the effective mass density $\bar{\rho}$.

Normal displacement decomposition and relationship to propagative and evanescent modes

The normal displacement $W(x)$ can be decomposed into two components

$$W(x) = \langle W \rangle + \delta W(x) \qquad (2)$$

where $\langle W \rangle \equiv \frac{1}{\pi R^2} \int_0^{2\pi} \int_0^R W(r, \phi) \, r dr d\phi$ is the surface-averaged normal displacement. Here, r and ϕ are the in-plane radial and azimuthal coordinates, respectively, and R is the DMR's radius. $\langle W \rangle$ can be described as the component representing the piston-like motion,

whereas $\delta W(x)$ comprises the high-spatial-frequency components after the average component is subtracted off. The spatial variation of $\delta W(x)$ can be delineated by the Fourier wave vectors $k_\parallel$ in the plane of the membrane, whose magnitude necessarily satisfies the inequality $|k_\parallel| \geq 2\pi/R$. Because normal displacement is continuous across the membrane-air interface and because the acoustic wave in air must obey the dispersion relation given by

$$k_\parallel^2 + k_\perp^2 = (2\pi/\lambda)^2 \qquad (3)$$

where $k_\perp$ is the normal component of the wave vector and λ is the wavelength, it follows directly from Eq. 3 that $k_\perp$ is imaginary for $\delta W(x)$ because $\lambda \gg R$ at the relevant frequencies. This fact implies that $\delta W(x)$ only couples to evanescent waves. In contrast, $\langle W \rangle$ is a constant and, therefore, its Fourier $k_\parallel$ components have a distribution that peaks at $k_\parallel = 0$. Hence, $\langle W \rangle$ couples to propagating waves (that is, reflected and transmitted waves). These are schematically illustrated in

Fig. 3C. It follows that, as far as the far-field wave scatterings are concerned, the DMR can be effectively viewed as a one-dimensional system (that is, solely determined by its $\langle W \rangle$) (14, 22).

Effective mass density and impedance of the membrane resonator

The above observations enable the determination of $\bar{\rho}$ in a simple manner

$$\bar{\rho} = -\frac{1}{\omega^2 \bar{d}} \frac{\langle P \rangle}{\langle W \rangle} \qquad (4)$$

where $\langle P \rangle$ is the surface-averaged pressure difference on two sides of the membrane, $\langle \ddot{W} \rangle = -\omega^2 \langle W \rangle$ is the surface-averaged acceleration, and $\bar{d}$ is the mean thickness. The result is plotted as a function of frequency in Fig. 3D. $\bar{\rho}$ becomes zero at the DMR's eigenfrequencies, across which it has different signs. This is of course associated with the phase difference of π on two sides of a resonance, with the negative $\bar{\rho}$ value implying that the system's acceleration opposes the external force. $\bar{\rho}$ can be related to the impedance of the DMR, defined as $Z = \langle P \rangle / \langle \dot{W} \rangle = i \langle P \rangle / \omega \langle W \rangle = -i \omega \bar{\rho} \bar{d}$. Thus, a near-zero $\bar{\rho}$ indicates that the effective impedance can be well matched to the air's impedance, which would allow DMR to optimally couple with the incident sound. Furthermore, because the Green function $G = \langle W \rangle / \langle P \rangle = i / \omega Z = -1/(\omega^2 \bar{\rho} \bar{d})$ (31), a near-zero $\bar{\rho}$ means that the normal displacement can diverge in the absence of dissipation. Thus, we expect a large transmission peak when $\bar{\rho}$ crosses zero at ~230 Hz, as shown in Fig. 3D. Near-zero $\bar{\rho}$ has also been utilized to achieve supercoupling, which allows an almost-perfect transmission through small channels under normal incidence (37–39). From the relations of $\bar{\rho}$ with the

impedance and the Green function, the imaginary part of $\bar{\rho}$, which is associated with dissipation, must be positive. This can be seen from its relation with Z, whose real part is associated with dissipation and, therefore, must be positive.

In the frequency regime between the two resonant peaks, we can find a particular point known as the antiresonance, as described previously. Because $\langle W \rangle = 0$ at the antiresonant frequency, $\bar{\rho}$ diverges in conjunction with a change in sign. When that happens, the impedance also diverges, and the wave would be totally reflected. This is observed as a transmission dip near 440 Hz in Fig. 3D. Such characteristic enables the realization of superthin lightweight reflective panels, which excel at blocking low-frequency noise (36, 40–44).

A somewhat nonintuitive result is that $\bar{\rho}$ is negatively divergent in the static limit. This originates from the fixed boundary condition of the membrane, which mandates $\langle W \rangle \to 0$. Under a quasi-static force, this imitates an infinite inertia of the system. The negative sign, however, is a reflection of Newton's third law: reaction opposes applied force. Such behavior of $\bar{\rho}$ is also manifested in other types of structures (27, 45). In particular, a negative $\bar{\rho}$ in the low-frequency limit was recently identified for liquid foam, which could be modeled as an array of flexible membranes (46).

Effective bulk modulus of two coupled membrane resonators and double negativity

As mentioned previously, the membrane's small thickness means that the vibrations involving the compression and expansion of the membrane along its thickness direction must occur at the very high-frequency regime. Such vibrations, however, are monopolar in character and, therefore, can give rise to anomalous values of $\bar{\kappa}$. To lower the monopolar resonant frequencies, one can couple two membranes to form a new DMR, as shown in Fig. 4A. This structure
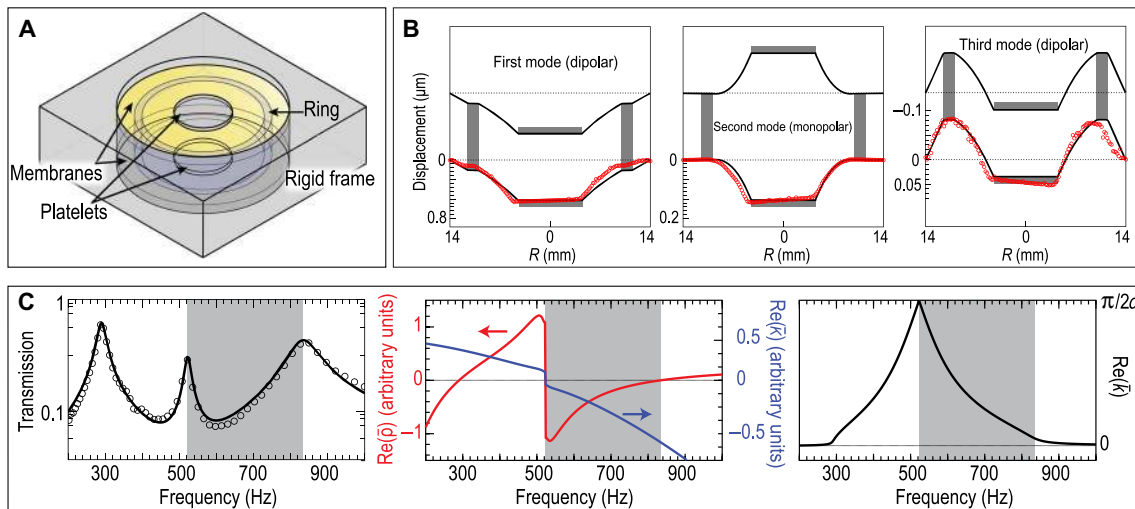
Fig. 4. Coupled membranes giving rise to both mass and modulus dispersions. (**A**) A schematic drawing of a DMR with two coupled membranes. Two identical membranes decorated with platelets are placed closely together, sealing a layer of gas in between. A rigid ring is added for extra tunability. (**B**) Normal displacement profiles of three low-frequency eigenmodes. Red symbols delineate the measured profiles using the laser vibrometer, whereas the black solid curves are the results of finite-element simulations. (**C**) Left: The transmission coefficient of the structure shown in (A), plotted as a function of frequency. Here, the circles denote the measured result, and the solid curve indicates the calculated result. Middle: Effective mass density $\bar{\rho}$ and bulk modulus $\bar{\kappa}$, plotted as a function of frequency. Right: The real part of the effective wave vector $\bar{k} = \omega \sqrt{\bar{\rho}/\bar{\kappa}}$, plotted as a function of frequency. The total thickness of the DMR is $2d$. Double negativity is seen in the region shaded in gray (22). The effective parameters here are extracted using the method detailed in Yang et al. (31).

has two dipolar eigenmodes similar to those of a single DMR; therefore, the characteristics of $\bar{\rho}$ are largely preserved. However, a new mode is produced, in which the two membranes oscillate against each other. The vibration profiles of these three modes are shown in Fig. 4B. For the new mode, it is clear that the DMR undergoes compressive/expansive motions, with its volume pulsating but with the center of mass remaining stationary. This mode leads to an effective bulk modulus $\bar{\kappa}$ that is frequency-dispersive (Fig. 4C, middle). $\bar{\kappa}$ reaches zero at the monopolar eigenfrequency and turns negative on the higher-frequency side of this mode. The dipolar and monopolar modes in this DMR are separately tunable. For example, in the study by Yang *et al.* (*22*), the monopole mode is located in the vicinity of a dipolar antiresonance. Because of the near-zero $\bar{\kappa}$, the characteristic impedance Z of the homogenized structure, comprising the two DMRs plus the air space in between, is given by $Z = \sqrt{\bar{\rho}\bar{\kappa}}$ and can have a magnitude that matches that of air, in spite of a large $\bar{\rho}$. When $\bar{\rho}$ and $\bar{\kappa}$ are both negative, the effective wave vector $\bar{k} = \omega\sqrt{\bar{\rho}/\bar{\kappa}}$ is real, implying a propagating wave. Furthermore, the real part of the effective index $\bar{n} = v_0/\sqrt{\bar{\kappa}/\bar{\rho}}$ must take the negative sign, where v_0 denotes the speed of sound in air. This can be seen by allowing a small imaginary part in $\bar{\kappa}$, which must be negative because $P \sim \bar{\kappa}\langle W \rangle$ and hence $\bar{\kappa} \sim 1/G'$, which differs from $\bar{\rho} \sim -1/G$ by a minus sign. Because the sign of the imaginary part of the Green function must be fixed, it follows that the imaginary parts of $\bar{\kappa}$ and $\bar{\rho}$ are opposite in sign. As the imaginary part of $\bar{\rho}$ is positive, as noted previously, $\bar{\rho}$ is in the second quadrant of the complex plane whereas $\bar{\kappa}$ is in the third quadrant. Therefore, $\bar{\rho}/\bar{\kappa}$ must lie in the fourth quadrant. For a forward-propagating wave in a medium with no gain, the imaginary part of the index must be positive. This mandates that the real part of $\bar{n}$ is negative as a result. In Fig. 4C (middle), both $\bar{\rho}$ and $\bar{\kappa}$ are negative in the gray-shaded region. Hence, a negative acoustic index can be achieved in a finite frequency range.

From the above discussion, we can see that even though the effective density is large at around 520 Hz (Fig. 4C, middle), a transmission peak is observed (Fig. 4C, left). Note that the maximum $\mathrm{Re}(\bar{k})$ can reach $\pi/2d$ at the monopole eigenfrequency (Fig. 4C, right), where $2d$ is the total thickness of the coupled DMR. Given the small thickness of the DMR, this is much larger than the wave vector allowed in free space (that is, $k \leq 2\pi/\lambda$). Such large wave vectors can, in principle, be utilized for a wide range of functionalities such as subdiffraction focusing. Various examples of these functionalities are described in "Superresolution and Focusing Beyond the Diffraction Limit."

SUPERRESOLUTION AND FOCUSING BEYOND THE DIFFRACTION LIMIT

Resolution limit and the evanescent waves
The exotic constitutive parameter values enabled by the acoustic metamaterials, such as DMRs, have expanded the horizon of acoustic wave manipulation. Among the many topics in wave physics, focusing and imaging have always occupied a central position, and an important issue here is the resolution limit, which arises from the basic constraint imposed by the dispersion relation: $k^2 = (\omega/v)^2 = (2\pi/\lambda)^2$. The magnitude of any real component of $\boldsymbol{k}_\parallel$ is therefore bounded by ω/v. Here, $\boldsymbol{k}_\parallel$ denotes the wave vector in the plane of the image. However, because $k^2 = \boldsymbol{k}_\parallel^2 + k_\perp^2$ (where $k_\perp$ denotes the wave vector component

perpendicular to the image plane), by allowing $k_\perp^2$ to be negative (with $k_\perp$ being purely imaginary), one can expand the magnitude of the allowed $\boldsymbol{k}_\parallel$ components to values larger than $2\pi/\lambda$, thereby enhancing the resolution of the image. However, the wave components with imaginary $k_\perp$ are the evanescent waves, which decay exponentially as a function of distance away from the source/scatterer. Consequently, details of a source/scatterer on the scale $\delta < 2\pi/k_{\max} = \lambda$ are lost in the far field and do not contribute to the image.

Reaching beyond the limit
The physics behind the diffraction limit is also informative on how to go beyond it. With the lack of detailed information from the source, intense focusing of energy into a subdiffraction scale remains possible by modifying the medium in the vicinity of the focal spot. Metamaterials potentially allow us to design the properties at will and therefore hold great promise in breaking the resolution limit. Lemoult *et al.* (*47*) reported an example of airborne sound. They built a two-dimensional square lattice of acoustic cavity resonators (soda cans). The system can be described by leaky modes, which arise from the interference between resonating and continuous fields, as indicated by the Fano-like resonance profile and the polariton-like dispersion (Fig. 5A). Here, we can observe an almost-flat dispersion immediately below the bandgap, implying large wave vectors attendant to a large density of states, which constitute the necessary elements for subdiffraction intense focusing (Fig. 5B). In addition, "defect modes" can be created by blue-shifting the resonant frequency of some chosen cavities of the bulk structure so that they fall into the bulk bandgap (Fig. 5A, gray region). As a result, the acoustic energy carried by these resonators was spatially confined in the lateral directions because there were no propagative modes within the bulk structure for these frequencies. Energy transport in the deep-subwavelength scale was thereby demonstrated by line defects, as shown in Fig. 5B (*48*).

In the above discussion, the subdiffraction focal spot is made possible by the extra wave vectors supplied by "rescaling" the diffraction limit near the position of the focus. To perfectly image a source, however, one has to capture the evanescent waves before they are lost. This generally requires focusing/imaging devices to operate in the near-field regime of the source. Then the question becomes, What should be the mechanism for sustaining the evanescent waves that convey the subdiffraction information?

The mismatch in momentum causes the loss of the high-spatial-frequency components in the far field because, for the propagating waves, the wave vectors are bounded by the free-space dispersion relation. One obvious path to sustaining the evanescent modes is to introduce extra momenta through lens design. Characterized by flat dispersions, local resonances can play such a role because the magnitude of $\boldsymbol{k}$ can extend to large values without changing the frequency (Fig. 5A). For example, owing to the longitudinal nature of acoustic waves, Fabry-Pérot resonances can be realized in waveguides with cross-sectional dimensions $\ll \lambda$, but which can have a length on the order of a wavelength or more. These resonances have almost-flat dispersions in which the magnitude of $\boldsymbol{k}$ can significantly exceed that of free space. By placing an array of these waveguides in the near field of the source, with each waveguide being capable of picking up highly localized disturbances and then conveying this information to the targeted locations, acoustic images with subwavelength sharpness have been achieved (*49*, *50*) (Fig. 5C).
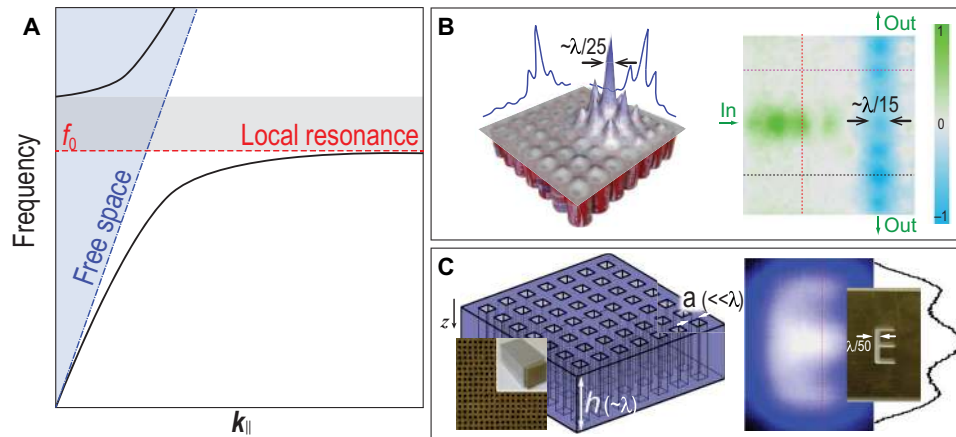
Fig. 5. Superresolution with local resonances. (**A**) The type of dispersion relation that is commonly used for superresolution and deep-subwavelength focusing with acoustic metamaterials. Here, the blue dotted-dashed line is the "sound line" (that is, the dispersion of acoustic wave in the homogeneous background medium), and the red dashed line is that of the local resonance with eigenfrequency f_0. Coupling between the two induces anticrossing in the vicinity of f_0 and gives rise to the dispersion delineated by the two black curves. The region shaded in gray is a bandgap. In free space, only the **k** components within the blue-shaded region are accessible. However, for the lower branch, the **k** components much larger than those available in free space (the blue-shaded region) become accessible. (**B**) Superresolution focusing (left; showing the pressure distribution) and subwavelength wave guiding (right; showing the normalized pressure amplitude) achieved by using a two-dimensional array of air-filled cavity resonators (soda cans). The resonances of the soda cans yield a dispersion, as shown in (A) (*47*, *48*). (**C**) A two-dimensional array of subwavelength waveguides is shown on the left. The thickness of the lens *h* is the same as the operating wavelength in air (not drawn to scale in this schematic drawing). These waveguides can support Fabry-Pérot resonances that have flat dispersions, which are useful for achieving superresolution imaging (*49*, *50*). In the imaging result shown on the right, light color represents stronger pressure intensity. The object is in the shape of the character "E" (inset). The stroke width of "E" is ~λ/50. The lens is placed close to the object, and an image is formed on the other side, where the shape "E" can be recognized (*50*).
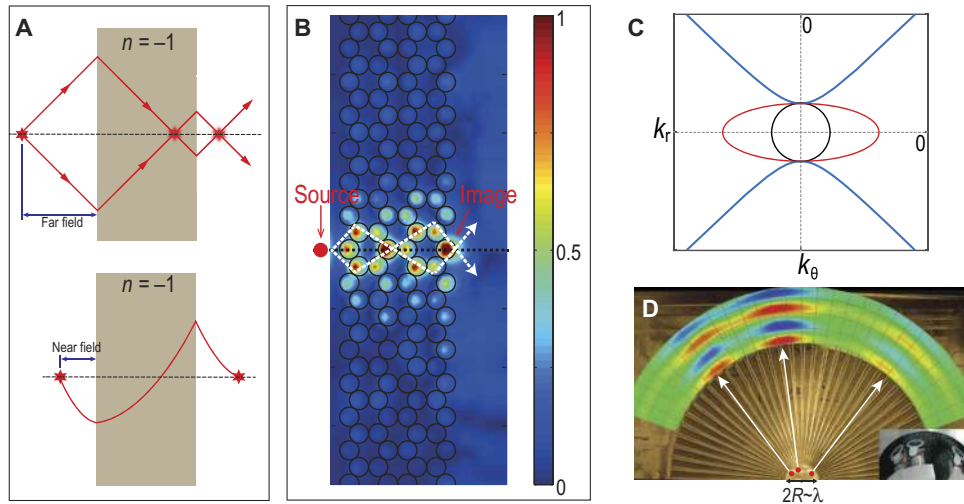
Acoustic superlens

A well-known scheme that promises perfect imaging is the superlens (*51*), which was proposed more than four decades ago in the context of electromagnetic waves—that a material with simultaneously negative permittivity and permeability (that is, negative index materials) can behave very differently from conventional materials. From Snell's law, it is easily seen that, at the interface between a conventional material and a negative index material, an obliquely incident wave on the side of the normal material can bend to the same side of the surface normal as the incident wave, inside the negative index material. Such "negative refraction" can cause a diverging wave to reconverge. It follows that a flat slab of the negative index material, when illuminated by a point source, can generate two foci: one inside the slab and another one on the other side of the slab (*52*). This is illustrated schematically in Fig. 6A (top). The first acoustic demonstration of negative refraction was reported by Zhang *et al.* (*53*). In this particular work, they built a metamaterial interface across which the effective index changed from positive to negative. A hot spot (that is, a focus) was clearly observed when a source was placed on one side of the interface.

The essence of a doubly negative superlens lies in the capture of information carried by the evanescent wave components, made possible by metamaterials. This is schematically illustrated in Fig. 6A (bottom). The amplification of evanescent waves can be achieved by using not only negative index materials but also singly negative materials alone because a surface-plasmon–like resonance can form at the interface between conventional materials and singly negative materials (*10*, *51*). For acoustic waves, Park *et al.* (*54*) used the negative $\bar{\rho}$ regime of a two-dimensional membrane array to show that the evanescent waves can indeed be amplified at the interface of metamaterials. Superresolution focusing was subsequently achieved

using a similar design (*55*). However, because the singly negative superlens relies on the interfacial mode that necessarily decays exponentially away from the interface, it is effective only when the thickness of the lens is subwavelength.

An acoustic doubly negative superlens was recently reported by Kaina *et al.* (*30*). The essence of the idea can be easily grasped by means of the tight-binding model. The coupling of two eigenstates with identical eigenfrequencies would give rise to anticrossing and yield two modes with opposite symmetries, separated in their resonant frequencies. On the basis of Helmholtz-like cavity resonators, which are known to generate monopolar modes and therefore negative $\bar{\kappa}$ values (*18*), two-dimensional lattices were constructed with a unit cell comprising a dimer of two coupled resonators. The coupling can be adjusted by either altering the distance between the resonators or introducing a slight mismatch in their eigenfrequencies, effectively tuning the frequency and intensity of the dipolar modes (two resonators out of phase). A narrow transparency band with negative dispersion is found inside the negative-modulus bandgap. With this design, a doubly negative flat lens was experimentally realized, with both foci inside and outside the lens clearly observed (Fig. 6B). The experiments also unambiguously showed that evanescent waves could indeed be amplified by the resonators and that imaging with subdiffraction resolution could be achieved. It is worth pointing out that the focal spot has a sharpness (with an amplitude full width at half maximum of λ/15) that is even smaller than the size of the imaged source (λ/5). This extra sharpness is again due to the relatively flat dispersion of the superlens' doubly negative band, which yields a high density of states and the attendant extra wave vectors.

A superlens does not change the decaying destiny of the evanescent waves once they leave the superlens (*56*). For this disadvantage to be overcome, a far-field superlens can be made by adding subwavelength

Fig. 6. Acoustic realizations of superlens and hyperlens. (**A**) Top: A slab of doubly negative medium can bring diverging waves into two foci: one inside the slab, and the other one outside. Bottom: The same slab can amplify evanescent waves, thereby theoretically enabling the formation of a perfect image. (**B**) Experimental demonstration of the imaging capability of an acoustic superlens (30). Here, cavity resonators (soda cans, represented by black circles) were arranged into a honeycomb lattice. It is clearly seen that the near field was sustained and even amplified by the metamaterial slab. Negative refraction and the consequent foci are delineated by white dashed arrows. The normalized pressure intensity field is displayed as a color map. The source (red dots) had an amplitude full width at half maximum of $\lambda/5$, whereas the measured image size was $\lambda/15$. (**C**) Three distinctive equifrequency contours. The black circle represents that of a homogeneous material. Anisotropy along $\hat{r}$ and $\hat{\theta}$ can distort the contour into an ellipse (red), in which a large k_r can be accessed. However, if the material's parameter is negative along $\hat{\theta}$ but positive along $\hat{r}$, then the contour becomes hyperbolic, wherein k_r and k_θ are no longer bounded (blue curves). (**D**) The strong anisotropy in k_r and k_θ, such as that indicated by the red ellipse in (C), used for superresolution imaging, as shown experimentally in Li *et al.* (63). Here, the fan-like structure has stripes alternating between air and brass. From the effective medium theory, the effective mass is highly anisotropic along the $\hat{r}$ and $\hat{\theta}$ directions. The center circle of the device has a diameter of about one wavelength, in which three sound sources were closely placed with subwavelength separations, represented by the red dots. An image of the sound sources is also shown in the lower-right inset. Red/blue represents positive/negative pressure, with the three clearly resolved regions being representative of the magnified image of the three sound sources.

structures (in the context of electromagnetic waves), such as gratings or corrugations (57, 58), to supply the additional lateral wave vectors that bring the evanescent waves (whose lateral wave vectors are larger than $2\pi/\lambda$ in magnitude) back into the light cone of the free-space propagating waves. However, so far, a working example for acoustic waves remains lacking.

Acoustic hyperlens

An alternative approach to superresolution is the hyperlens (59). The basic concept can be easily grasped by considering the two-dimensional configuration. If one of the effective constitutive parameters, say $\bar{\rho}$, is negative along the radial direction $\hat{r}$ but positive along the azimuthal direction $\hat{\theta}$ (that is, $\bar{\rho}_\theta \bar{\rho}_r < 0$), then the dispersion relation $k_\theta^2/\bar{\rho}_r + k_r^2/\bar{\rho}_\theta = \omega^2/\bar{\kappa}$ is hyperbolic in shape, as shown in Fig. 6C.

Such a dispersion was shown to be possible for acoustic waves (60–62). As a result, k_θ and/or k_r is no longer bounded and can, in principle, take arbitrarily large values and still satisfy the hyperbolic dispersion relation without requiring any of the wave vectors to be imaginary. Approximating this idea, Li *et al.* (63) demonstrated acoustic superresolution in which $\bar{\rho}_\theta$ and $\bar{\rho}_r$ have the same sign but differ by a large ratio. The relevant structure is fan-shaped, with alternating brass and air stripes arranged along the $\hat{\theta}$ direction (Fig. 6D). Such a geometric structure implies that the effective $\bar{\rho}$ can be obtained as the arithmetic average of the two components' mass densities along $\hat{\theta}$ and as the average of the two components' inverse mass densities along $\hat{r}$. Because brass and air have hugely different mass densities,

these two effective mass densities can differ by a large ratio. As a result, the equifrequency contour in such a device is elliptical, with a large eccentricity. This allows access to large $\boldsymbol{k}$ components. Such a device can realize superresolution without the need for negative parameter values, which are inevitably the consequence of resonances (and therefore can only be effective over a narrow frequency range). Hence, its functionality is effectively broadband. In Fig. 6D, three sound sources placed inside the inner circle of the fan-like structure, with a separation that is four to seven times smaller than the relevant wavelength, were seen to be clearly separated and magnified when measured outside this hyperlens, indicating the successful conversion of evanescent waves into propagating waves. An acoustic hyperlens with true hyperbolic dispersion was recently demonstrated using metamaterial elements similar to membranes (62), which are known to generate negative $\bar{\rho}$ values.

TRANSFORMATION ACOUSTICS AND DEVICES WITH SPATIALLY VARYING INDEX

Determining constitutive parameter functions through coordinate transformation

The advent of acoustic metamaterials has greatly expanded the allowed values of the constitutive parameters. A generalized way to appreciate the implied capabilities afforded by this new freedom is through transformation acoustics, following the example of

transformation optics (64–67). Consider the time harmonic acoustic wave equation

$$\nabla \cdot [\overleftrightarrow{\rho}(\boldsymbol{x})^{-1} \nabla P(\boldsymbol{x})] = -[\omega^2 / \kappa(\boldsymbol{x})] P(\boldsymbol{x}) \qquad (5a)$$

where $\overleftrightarrow{\rho}(\boldsymbol{x})$ denotes the mass density tensor. If one applies a coordinate transformation $\boldsymbol{x}'(\boldsymbol{x})$ to map each point $\boldsymbol{x}$ to a corresponding point $\boldsymbol{x}'$ in another space, then the acoustic wave equation in the new space retains the same form

$$\nabla' \cdot [\overleftrightarrow{\rho}'(\boldsymbol{x}')^{-1} \nabla' P(\boldsymbol{x}')] = -[\omega^2 / \bar{\kappa}'(\boldsymbol{x}')] P(\boldsymbol{x}') \qquad (5b)$$

in which the constitutive parameters transform to the effective parameter values given by $\bar{\kappa}'(\boldsymbol{x}') = [\det A]\kappa(\boldsymbol{x})$ and $\overleftrightarrow{\rho}'(\boldsymbol{x}') = A[\overleftrightarrow{\rho}(\boldsymbol{x})]A^{\mathrm{T}} / \det A$. Here, A is the Jacobian matrix of coordinate transformation, A^{T} is its transpose, and $\det A$ denotes its determinant. If there are no limitations on the values of the effective constitutive parameters, then we can design materials that can manipulate waves in almost any way we desire by changing the coordinate system (66, 68). Among the kaleidoscope of functionalities made possible by acoustic metamaterials in conjunction with transformation acoustics, cloaking is perhaps the most remarkable example. Norris (69) recently conducted a comprehensive review of this topic. Below, we briefly survey some important results.

Acoustic cloaking

An obvious cloaking strategy is to avoid scattering by guiding the wave around the object. Theoretical and numerical works showed that such a scheme is in fact possible for acoustic waves (70–73). A particularly simple example of cloaking is to expand a point into a spherical shell, with a and b denoting the inner and outer radii of the shell, respectively. The relevant effective density and modulus have the following forms

$$\bar{\rho}'_r(r') = \rho_0 \frac{b-a}{b} \left(\frac{r'}{r'-a} \right)^2 \qquad (6a)$$

$$\bar{\rho}'_\theta = \bar{\rho}'_\phi = \rho_0 \frac{b-a}{b} \qquad (6b)$$

$$\bar{\kappa}'(r') = \kappa_0 \left(\frac{b-a}{b} \right)^3 \left(\frac{r'}{r'-a} \right)^2 \qquad (6c)$$

Here, ρ_0 and κ_0 denote the constant constitutive parameter values of the original homogeneous medium, whereas r, θ, and ϕ (also r', θ', and ϕ') represent the radial, azimuthal, and polar coordinates, respectively. Such a cloaking shell, if realized, can totally isolate sonically the object placed inside the sphere of radius a. However, the parameter values required by Eqs. 6a to 6c are very extreme and hence not likely to be realized perfectly. Another important point to remember is that, so far, the effective parameter values realized by acoustic metamaterials have been frequency-dispersive; hence, it can mean that cloaking occurs only within a narrow frequency range. The first functional cloaking device was achieved with water-borne ultrasound. In this work by Zhang *et al.* (74), the scatterer was covered by a metallic

cylindrical shell engraved with an interconnected network of subwavelength cavities. The effective parameters of this structured shell were graded along the radial direction. Experimental observations showed a clear reduction in shadowing, which is a decisive evidence of cloaking.

Another strategy is the so-called ground-plane cloak, which hides scatterers placed on a flat reflective surface. Owing to the nearly two-dimensional geometry and the consequent removal of the extra geometric constraints, the requirements for material parameters become easier to realize (75). Such cloaks were indeed demonstrated for airborne sound (76, 77). The cloaks were made of layers of plastic thin plates perforated with an array of subwavelength holes. They were assembled into a pyramidal shape, similar to a tent covering the scatterer that was placed on a hard reflecting surface. The cloak had a designed distribution of effective mass density and modulus. In particular, the mass density was anisotropic but uniform along each direction. Experiments confirmed a clear reduction in scattering, in spite of an impedance mismatch between the cloak and the air. Modified versions were also demonstrated to hide objects placed with some geometric restrictions (78, 79). Alternatively, careful arrangement of additional scatterers around an object can result in the cancellation (by interference) of the original scattered waves (80–83), leading to the cloaking effect.

Zero-index medium

Zero-index medium (ZIM) can also be used for cloaking. The physics of such materials can be easily grasped from two distinct points of view. Phenomenologically, $\bar{n} \approx 0$ indicates that the wave phase does not advance inside the material because $\Delta\phi = \bar{k}d = \bar{n}\omega d/c \approx 0$, where $\Delta\phi$ is the accumulated phase of a wave with an angular frequency ω passing through a distance d. From the point of view of transformation acoustics, an area/volume occupied by such materials is equivalent to a point with a measure of zero but expanded in space (66). A consequence is that the wave field inside such materials will not undergo any change and, therefore, must be constant. This also means that the outgoing wavefront is determined by the shape of the ZIM's boundary. Hence, a scatterer placed inside a ZIM is hidden, in the sense that it generates no scattered wave if viewed from the outside (84).

However, it was subsequently realized that ZIM can have some interesting hiccups. For example, a plane wave passing through a slab of ZIM with thickness d would accumulate no phase. However, the same wave propagating through the background medium with a refractive index n would advance in phase by $\Delta\phi = n\omega d/c$. It is easy to see that the apparent phases of the outgoing waves in these two cases are different unless $d = 2m\pi \frac{c}{n\omega}$, where m is an integer. This puts a constraint on the thickness of a perfect ZIM cloak because, otherwise, the cloaking effect would be lost through a comparison of the phases. Moreover, ZIM cloaking can only happen with normal incidence. A wave with oblique incident angles will encounter total "internal" reflection at the interface. This interesting characteristic can in fact be turned into an advantage. A simple example is a prism made with ZIM, in which the two boundaries make a nonzero angle. If one boundary of this prism is parallel to an incoming wavefront (that is, normal incidence), total transmission through both prism interfaces is expected. However, a wave propagating in the reverse direction (to that of the incident wave) would see a nonzero incident angle and therefore is totally reflected by the prism. Asymmetric transmission can be realized by this restricted geometry (85). Reciprocity is not broken in the system (more details on this matter will be discussed in "Nonreciprocal Acoustic Devices"). In addition, a ZIM's functionality is

highly sensitive to the nature of defects. Wave behaviors inside a ZIM are ultimately governed by the wave equation and the relevant boundary conditions. Imagine a defect with an acoustically soft boundary (defined as $P = 0$) placed inside a ZIM. This would mandate the wave field inside to be zero everywhere, thereby causing total reflection of the incident waves (86–88). Recently, it was proposed that this boundary dependence of ZIM in the elastic wave context be used to mitigate the transverse-longitudinal mode conversion of scatterers, which was ubiquitous for traditional elastic materials (89).

## Acoustic "black hole" and "illusion" devices

Besides cloaking, transformation acoustics also proves to be a powerful tool for designing a wide range of acoustic functionalities. Opposite to the functionality of a cloak, which detours the incident wave around a scatterer, a device can be designed to guide the incident wave into the core region without being scattered. By placing absorbing agents in the core region, these acoustic "black holes" can display absorption performance independent of the incident angle (90–92). A number of different acoustic "illusions" also demonstrate the power of transformation acoustics. An example is an acoustic wavefront rotator. In a two-dimensional cylindrical geometry, the design follows a transformation only in the azimuthal coordinate: $r' = r$; $\theta' = \theta$ for $r > b$, $\theta' = \theta + \theta_0$ for $r < a$, and $\theta' = \theta + \theta_0 \frac{b-r}{b-a}$ for $a < r < b$, where a and b are the inner and outer radii of the annular region occupied by the device, respectively. This coordinate transformation is then mapped to the mass density tensor of the device. Such a device was experimentally realized and demonstrated to be capable of rotating

a planar wavefront by an angle θ_0 in the region $r' < a$, which created an illusion of the incident angle (93). Similarly, this design was used to alter the radiation directivity of a sound source that was enclosed inside (94). A more sophisticated illusion was experimentally demonstrated, in which the scattering of a cylinder was reshaped into that resembling the scattering by a block (78). Some other examples, such as aberration correction (95) and radiation collimation (96), were investigated with theory and numerical simulations.

SPACE-COILING AND ACOUSTIC METASURFACES

Incurring large phase delays within a small space

Acoustic waves are longitudinal in character. Hence, acoustic waveguides have no cutoff frequency. This feature can be exploited to be an advantage in the design of acoustic metamaterials. Liang and Li (84) proposed a design with complex labyrinth passages that are deep subwavelength in their cross sections. Dubbed "space-coiling," this design essentially forces sound waves to propagate through passages that are much longer than their external dimension. An example is shown in Fig. 7A. The coiled-up passage introduces a large phase delay $\Delta\phi = k_0 L$, where k_0 is the wave number in the background fluid and L is the "acoustic path." Historically, similar structures have found applications in bass woofers that were sometimes called folded-horn speakers, a name that aptly describes the enclosure design (97). By adjusting the total length of the passage, one can tune the apparent phase and group velocities and hence the effective index and the dispersion
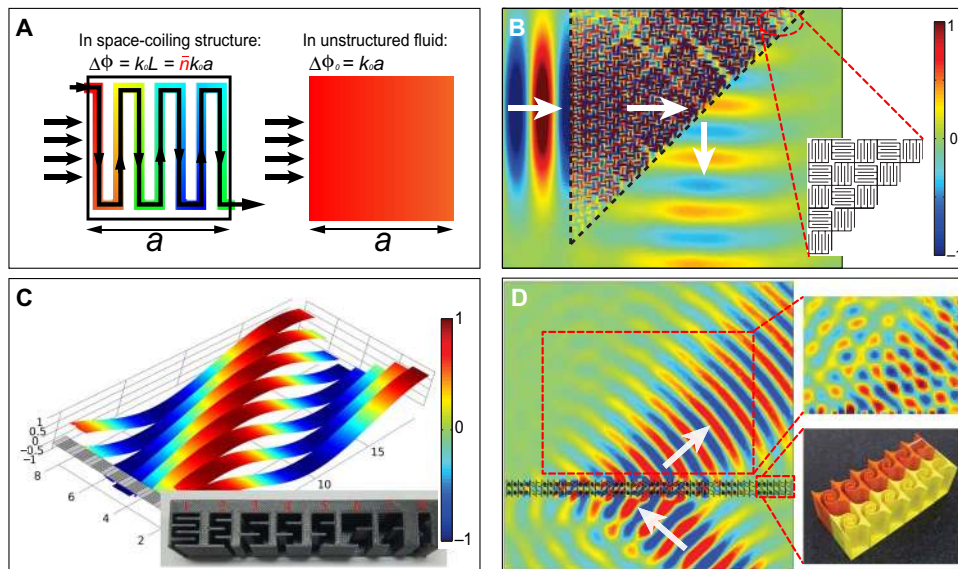
Fig. 7. Space-coiling and acoustic metasurfaces. (**A**) An example of the space-coiling structure and the relevant sound pressure field inside (84). The color indicates the phase of the propagating sound wave. Here, a large phase delay $\Delta\phi \gg \Delta\phi_0 = k_0 a$ can be caused by the coiled channels, where k_0 is the wave vector in the background fluid and a is the exterior dimension of the cell. With proper design, such structures can be used for many novel effects, such as the negative-refracting prism shown in (**B**) (84). Here, space-coiling unit cells are assembled into a prism. Sound incidents from the left, and encounters of negative refraction as it emerges from the prism, are indicated by white arrows. Red/blue represents positive/negative pressure. (**C**) A design of reflective acoustic metasurface that is capable of generating phase changes up to 2π. This can be seen from the color (red and blue represent positive pressure and negative pressure, respectively) and the undulations of the stripes (108). The metasurface is shown on the lower left, and the wave is incident normally on the surface. The ridge of red stripe sections indicates the emergence of a reflected wave at a nonspecular angle. Inset: Implementation of a slightly modified space-coiling design of the metasurface, with a lateral gradient of phase delays (109). (**D**) A design of the metasurface that generates negative refraction for the transmitted wave. Left: The simulation result (white arrows delineate incident and refracted beam directions). Right: The experimentally measured pressure map (113) (red and blue represent positive pressure and negative pressure, respectively) (top) and a photographic image of a section of the actual sample (bottom).

relation. Novel effects such as negative refraction (Fig. 7B), near-zero-index cloaking, and Dirac-like dispersion were envisioned. Subsequent experiments proved the effectiveness of this concept (*98–100*).

Because of its effectiveness and ease of implementation, the space-coiling design has attracted considerable attention immediately after its initial proposal. Functionalities such as zone-plate focusing (*101–104*), one-way transmission (*85*), high transmission (*103, 105*), and high absorption (*106*) were successfully demonstrated. In a recent paper, Cheng *et al.* (*107*) reported a cylindrical unit cell with fan-shaped space-coiling segments. The winding air passage gave the unit cell a high effective index, thereby allowing multiple Mie-like resonances of distinct angular momenta. Single negativity in $\bar{\rho}$ and $\bar{\kappa}$ was shown to be possible. Its strong resonant features also enabled a large scattering cross section, which led to a high reflection even with sparsely positioned units.

Acoustic metasurfaces for phase manipulations

Space-coiling structures are particularly effective for constructing "acoustic metasurfaces." These are essentially acoustic phase arrays with subwavelength thickness, which are capable of generating an abrupt phase shift (up to 2π) across a single layer. This phase shift supplies the incident wave with an extra momentum, thereby causing it to reflect/refract at an "abnormal" angle. A feasible design was proposed by Li *et al.* (*108*) in a reflective geometry (shown in Fig. 7C) in which part of the incident wave can enter the coiled channels, which are designed in such a way that the reflected wave would acquire a laterally varying phase delay so that a nonspecular reflected beam can appear. The wavefront of the latter can be identified by the red ridge in Fig. 7C. Experiments quickly followed (*109*), in which the intriguing effects (including negative refraction, focusing, and surface wave conversion) were observed. One drawback of the space-coiling structures is the large impedance mismatch to the incident wave. That can mean some challenges for the transmission configuration because, in addition to phase shifts, impedance matching is also required to achieve optimal results. This point was considered in some theoretical works (*110, 111*). Recent experimental demonstrations have sought to improve impedance matching by adding horn-like designs (*112–114*) (Fig. 7D, inset) or by using resonances (*115, 116*) to improve coupling. In particular, in Fig. 7D, negative refraction was demonstrated in transmission by using a lateral gradient in phase delays. However, some of these designs somewhat sacrificed the thickness of the devices (which is close to $\lambda/2$) in exchange for better performance. Li *et al.* also demonstrated complex wavefront shaping, such as the formation of self-bending beams, by imprinting spatial functions to the phase profile generated by the metasurface. However, these exotic functionalities are dependent on the conditions of the incident wave such as the beam shape, incident angle, and source geometry and position (*109, 116*).
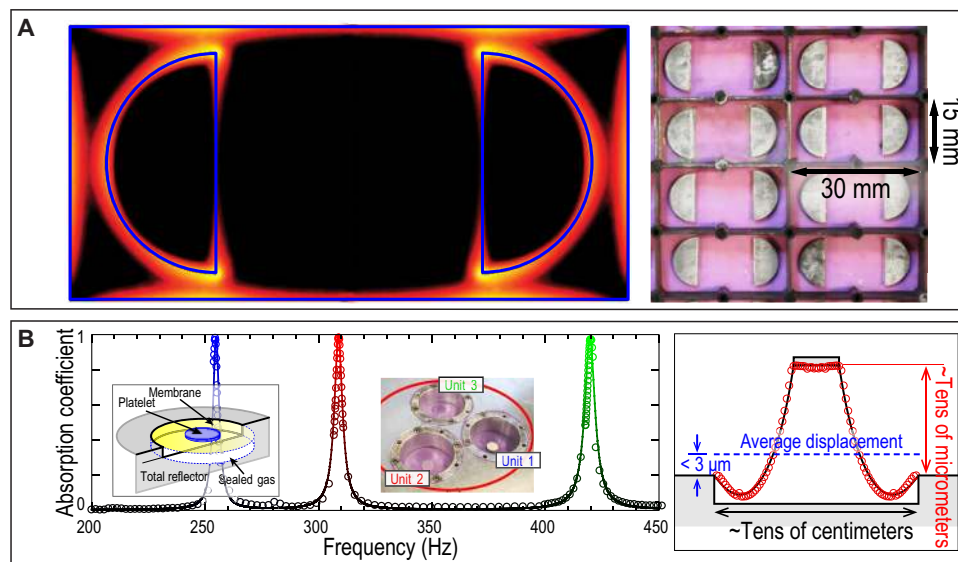
ABSORPTION

Acoustic absorption is important for both noise mitigation and interior acoustics optimization. Two elements are central to absorption performance. First is an effective means for dissipation. A most straightforward strategy is through friction. Hence, porous materials such as sponges, mineral wools, fiber glass, and cotton are commonly used as sound-absorbing materials (*117*). Second is impedance matching, which enhances coupling of the incident acoustic energy with the absorbers. To this end, gradient index is a standard method

used to improve absorption performance. For example, porous materials are prepared with spatially varying filling density, and blocks of absorbing materials are cut into wedge or conical shapes to improve impedance matching (for high-frequency sound, this also adds the benefit of a diffusor). In addition to these two elements, resonances can also be advantageous because they are usually accompanied by high energy density and improved impedance matching. Microperforated panels with back cavities constitute an example along this line (*118*).

The abovementioned examples generally show good absorption performance for a relatively broad range of frequencies. However, they become less effective in the low-frequency regime. The reasons are both fundamental and practical. Dissipation in linear response systems is necessarily quadratic in rates; therefore, absorption is intrinsically weak at low frequencies. A straightforward way to enhance absorption is to use a large amount of absorptive materials—typically with a thickness on the order of several wavelengths. This is usually an impractical scenario for low-frequency sound, whose wavelength can exceed 1 m. Acoustic metamaterials bring a new perspective to this traditional challenge. With proper design, energy density within subwavelength resonators can reach a very high level. Because absorption is proportional to the product of energy density and the absorption coefficient, the small magnitude in the latter (in the low-frequency regime) can be compensated for by a large magnitude in the former. An example of large absorption is reported in a study by Mei *et al.* (*119*), in which elastic membranes of submillimeter thickness were decorated by asymmetrically shaped rigid platelets. Because of the contrast in flexural rigidity at resonances, a large energy density can be concentrated within small regions near the perimeter of the rigid platelets (Fig. 8A). These regions have lateral dimensions that are much smaller than the relevant wavelength. Hence, the high energy densities are decoupled from the propagating modes (see Eq. 2 and the argument related to δW) and can only be absorbed. Further investigations revealed that high local energy density and perfect impedance matching can be simultaneously attained (*120*). The idea is to hybridize the two low-frequency eigenmodes of a DMR (Fig. 3B) in the formation of a new resonant mode by adding a thin layer of sealed gas behind the DMR (Fig. 8B, left). Because the hybridized mode profile is necessarily the linear superposition of the two low-frequency eigenmodes, the two components of the normal displacement, $\langle W \rangle$ and $\delta W(\boldsymbol{x})$ in Eq. 2, become separately tunable degrees of freedom. It is then possible to optimize $\langle W \rangle$ for perfect impedance matching to air, whereas $\delta W(\boldsymbol{x})$ can be very large so as to absorb all the incident wave energy (Fig. 8B, right). This combination leads to a low-frequency narrow-bandwidth total absorber with an extremely small thickness.

Various alternative concepts also show good promise. An ultrathin resonant absorber with a design concept similar to space-coiling was reported (*106*), in which sound was forced to go through a convoluted air passage for a distance on the order of $\lambda/4$ so that the total reflection was reduced. The thin air passage, which resembled a perforated plate, also served as the absorbing medium. Jiang *et al.* (*121*) demonstrated broadband absorption by stacking multiple quarter-wave resonators in a tapered manner. Originally studied in optics, coherent perfect absorption (CPA) arises from the destructive interference between counter-propagating waves, which can lead to the cancellation of outgoing waves and, thus, total absorption. Theoretical investigations suggest that CPA also applies to acoustics, albeit with stringent requirements on material properties and geometry (*122–125*). In particular, Leroy *et al.*

Fig. 8. Acoustic absorption by DMRs. (A) Left: Numerically simulated elastic bending energy density of a soft membrane decorated with rigid platelets, delineated by blue curves. Light color represents high energy density. The energy is highly concentrated in the small areas along the perimeters of the platelets and along the sample boundary (*119*). Right: A photographic image of such a membrane absorber. **(B)** Total absorption of low-frequency sound at multiple frequencies using hybrid resonances. The left panel shows the absorption coefficient of a three-unit membrane metasurface (structure shown in the right inset). The markers are measured data, and the solid curve represents simulation. The membrane metasurface unit cell comprises a stretched membrane decorated with a rigid platelet, backed by a thin layer of sealed gas (thickness expressed in centimeters). The hybrid resonance structure is fabricated on top of a hard reflecting surface (left inset). The right panel of (B) shows the vibration profile of the membrane at the hybrid resonant frequency. Red markers represent experimentally measured data. The surface-averaged normal displacement (blue dashed line; not drawn to scale) matches the amplitude of the incident sound—an indication of impedance matching. However, the normal displacement can be much larger locally, suggesting a very large energy density in the form of the deaf component that couples only to evanescent waves (*120*).

(*125*) demonstrated high absorption in water-borne ultrasound by covering a sound reflector with a subwavelength layer of resonant "bubbles" that were hollowed in a soft polymer film. Degenerate critical coupling is another possible route for total absorption. It requires the exact degeneracy of two eigenmodes with different symmetries (*126*), a condition that can, in principle, be satisfied with proper metamaterial designs. A particular realization of total absorption by two degenerate resonators was recently reported (*127*), in which a monopolar resonator and a dipolar resonator, both deep subwavelength in scale and resonant at the same frequency, were placed closely together so that the incident wave perceived the two as a single unit. At resonance, the average impedance of the two subunits perfectly matched the air so that the incident wave generated no reflection, whereas the different symmetries of the two resonators caused the transmitted wave to be cancelled. That resulted in total absorption.

So far, the high absorption achieved by acoustic metamaterials remains within narrow frequency bands. It complements well the acoustic absorption of the traditional approaches in the low-frequency regime, where machine-generated noise can be an important source.

ACTIVE CONTROL

As "tuning" acoustic metamaterials usually amounts to the fabrication of new samples, reconfigurable metamaterials are important for their versatility and broadened application potentials. Indeed, increasing efforts have been drawn toward such designs. Certain nonlinear processes can introduce multistable configurations that are controllable by external means, such as static force loading. This was exploited to add

tunability to metamaterials. Successful examples were demonstrated with ordered granular chains/crystals (*128–130*) and buckling elastomers (*131, 132*). Piezoelectric elements, which have long been used for acoustic-electric transducers, can display an acoustic response that is variable under different external electric controls (*133–137*). Schemes based on the electrical control of resonant frequencies in membrane-type metamaterials have been proposed and realized (*138*).

Besides reconfiguration, powered devices are also exploited to achieve more exotic functionalities such as asymmetric scattering. These functionalities are partly derived from the controlling electronics. For example, Popa and Cummer (*137*) constructed a nonreciprocal acoustic device in which an electronic frequency converter was loaded onto a piezoelectric membrane, which gave it a nonlinear response that can up-convert the frequency of the incident sound. A Helmholtz resonator was then connected to one side of this membrane to filter the incident sound, leaving the up-converted frequency unaffected. This combination resulted in the strong asymmetric transmission of acoustic energy. Fleury *et al.* (*139*) treated an electronically controlled loudspeaker as a gain component, used to compensate for the energy that was lost to an absorber. This allowed the realization of anisotropic transmission resonance: for incidence from both sides, transmission reached almost unity, but because of the asymmetrically positioned gain and loss components, reflections were highly asymmetric.

EMERGING NEW DIRECTIONS AND OUTLOOKS

Acoustic metamaterials are rapidly evolving both in the diversity of functionalities and in new directions that may not fit the original

definition of acoustic metamaterials as constituted by resonant units, but nevertheless display characteristics that are beyond those found in nature.

Nonreciprocal acoustic devices

In recent years, many structures with cleverly designed spatial asymmetry have been demonstrated to display asymmetric transmission. However, asymmetric transmission and nonreciprocity are fundamentally different, in spite of some cursory similarities. An easy test for nonreciprocity, in the absence of dissipation and gain, is to time-reverse the outgoing waves and compare the waves formed on the other side of the sample with the original incident wave. If the two are not the time-reversed versions of each other, then we have nonreciprocity. More detailed discussions can be found in the studies of Maznev *et al.* (*140*) and Jalas *et al.* (*141*). Nonreciprocity can be acquired with relative ease in electronic and photonic systems, owing to their inherent sensitivity to magnetic fields whose presence breaks time-reversal symmetry. However, acoustic systems generally do not respond to magnetic fields, and new tricks are therefore needed to achieve similar effects. A feasible method is to use moving fluid. For example, the Aharonov-Bohm effect in electronic systems can be mimicked by performing a time-reversal acoustic experiment (in which sensed acoustic waves are time-reversed by computer and emitted back through the same transducers) in the presence of a water vortex (*142*). In a recent experiment, Fleury *et al.* (*143*) constructed a ring-shaped resonator in which the air was set into circulation. The flowing medium induced a strong Doppler effect, through which sound propagation was shown to be nonreciprocal among the three outlet ports. This is a system that breaks reciprocity and therefore enables true acoustic isolation. Incorporation of nonlinearity into acoustics has shown very interesting results such as reconfigurability (*130–132*), high-intensity focusing (*128*), and nonreciprocal transmission (*129, 137, 144–146*). Systems whose property (for example, effective mass) is temporally modulated are also able to display nonreciprocity (*147*).

Elastic and mechanical metamaterials

Acoustic metamaterials have also influenced the study of structural elastic waves in the past few years. For example, local resonances were shown to be effective for manipulating elastic surface waves (*148–151*). Cloaking (*152–155*), negative refraction (*156–158*), and subdiffraction focusing (*158, 159*) were demonstrated in thin plates. Several theoretical and numerical investigations on resonant elastic metamaterials revealed fascinating possibilities such as negative shear modulus (*21*) and superanisotropy (*20*). However, experimental efforts are still rare. A particularly ambitious target is the mitigation of the destructive effects of seismic waves. Recently, a full-scale seismic wave experiment was reported by Brûlé *et al.* (*160*), wherein a rectangular array of boreholes drilled into the ground surface showed the clear effect of blocking low-frequency surface vibrations.

Originally proposed by Milton and Cherkaev (*161*) and Milton (*162*), "pentamode" mechanical metamaterials represent a novel type of structural material in which rigidity is maintained through point contacts between the tips of the elongated structural elements. Because bending and rotational motions about these point contacts encounter much smaller resistances, these structures consequently can have a bulk modulus that is much larger than the shear modulus, leading to the interesting characteristic that the compression and transverse vibrations are essentially decoupled. The past few years have witnessed

the realization of pentamode metamaterials, thanks to new fabrication technologies such as lithography and three-dimensional printing (*163–166*).

Graphene-inspired metamaterials

The successful fabrication of graphene and the subsequent wave of research studies have sparked a tremendous interest in realizing, for acoustic waves, dispersion relations that are similar to those found in a semimetal electronic band structure known as the Dirac cone, featuring crossed linear dispersions at a point in the reciprocal space (*98, 167–171*). Such linear dispersions have several important implications. For example, a Dirac-like dispersion located in the Brillouin zone center (Γ point, where $k \sim 0$) is related to a near-zero refractive index (*169, 172*). Therefore, it can serve as a straightforward platform for the study of zero-index physics and relevant functionalities. In addition, Dirac-like dispersion is characterized by two (or more) states that can become degenerate. This is an indication that they have different types of symmetry. The evolution of symmetry for these isolated bands may be characterized by geometric phases and/or topological entities such as the Chern number. For example, the symmetry of Bloch states is closely related to the geometric phases of the bands, and their direct observation is easier in macroscopic systems such as phononic crystals (*173*). This is the reason that Dirac-like dispersion is usually a good starting point for the realization of relevant exotic physics, which has attracted significant attention in electromagnetism and optics, in particular for photonic crystals (*174*). Recently, topological transition was observed in one-dimensional phononic crystals (*173*). A number of theoretical works have investigated its potential realization in higher dimensions, including the unique chiral edge modes that are immune to backscattering (*175–181*). Because acoustic waves are insensitive to magnetic fields, which are crucial elements in the appearance of the chiral edge modes in graphene, artificial gauge fields of various types have been proposed to mimic the effect of magnetic fields in the context of acoustic metamaterials. Realizations of the chiral edge modes in mechanical systems have also appeared in systems such as a two-dimensional array of coupled pendula (*182*) and an oscillator array consisting of spinning masses (*183*). Recently, Weyl points have been observed in photonic crystals (*184*), and a proposal for its realization in acoustics has also been reported (*179*).

Acoustic metamaterials with characteristics describable by non-Hermitian Hamiltonians

Another new direction is the physics of non-Hermitian Hamiltonians, which describes systems with loss and/or gain (*185*). Originally studied in nuclear systems to explain phenomena such as the lifetime of excited states, real observable eigenstates have been shown to exist, despite the fact that the relevant eigenvalues may be imaginary. Intriguing phenomena related to exceptional points, at which two or more eigenstates coalesce when driven by a system parameter (such as loss) (*186*), have found applications such as asymmetric reflection (*187*), single-mode lasing cavity (*188*), and loss-induced lasing revival (*189*) in optical systems. Investigations in the context of acoustics have also started to appear (*139, 190, 191*).

An active field with a promising future

Acoustic metamaterials have undoubtedly expanded the capabilities of acoustic wave manipulation. Reliance on resonances implies frequency

dispersions and narrow frequency bands in the effectiveness of acoustic metamaterials. Hence, broadening the frequency range of operation of acoustic metamaterials is an obvious direction for solidifying their roles in diverse applications. Acoustic metamaterials are also expected to affect ultrasonic acoustics, where countless applications (such as medical imagining) lie. However, even in the present state of acoustic metamaterials, new thinking such as "digitizing" metamaterials into binary units (192) has already made some promised functionalities more accessible, such as actively controllable metasurfaces. Owing to the simplicity of the fabrication process (compared to those for electronic and display devices, for example), the commercialization of some of the research results targeting old challenges such as noise abatement and selective perception in human audition (193) may occur in the near future. Furthermore, can acoustic metamaterials be useful for protection against seismic waves? Such an obvious question demands answers, and they may not be too far away.

REFERENCES AND NOTES

1. E. Yablonovitch, Inhibited spontaneous emission in solid-state Ephysics and electronics. *Phys. Rev. Lett.* **58**, 2059–2062 (1987).
2. S. John, Strong localization of photons in certain disordered dielectric superlattices. *Phys. Rev. Lett.* **58**, 2486–2489 (1987).
3. M. Sigalas, E. N. Economou, Band structure of elastic waves in two dimensional systems. *Solid State Commun.* **86**, 141–143 (1993).
4. M. S. Kushwaha, P. Halevi, L. Dobrzynski, B. Djafari-Rouhani, Acoustic band structure of periodic elastic composites. *Phys. Rev. Lett.* **71**, 2022–2025 (1993).
5. E. Yablonovitch, T. J. Gmitter, Photonic band structure: The face-centered-cubic case. *Phys. Rev. Lett.* **63**, 1950–1953 (1989).
6. R. Martínez-Sala, J. Sancho, J. V. Sánchez, V. Gómez, J. Llinares, F. Meseguer, Sound attenuation by sculpture. *Nature* **378**, 241 (1995).
7. F. R. Montero de Espinosa, E. Jiménez, M. Torres, Ultrasonic band gap in a periodic two-dimensional composite. *Phys. Rev. Lett.* **80**, 1208–1211 (1998).
8. R. A. Shelby, D. R. Smith, S. Schultz, Experimental verification of a negative index of refraction. *Science* **292**, 77–79 (2001).
9. V. M. Shalaev, Optical negative-index metamaterials. *Nat. Photonics* **1**, 41–48 (2007).
10. N. Fang, H. Lee, C. Sun, X. Zhang, Sub-diffraction-limited optical imaging with a silver superlens. *Science* **308**, 534–537 (2005).
11. D. Schurig, J. J. Mock, B. J. Justice, S. A. Cummer, J. B. Pendry, A. F. Starr, D. R. Smith, Metamaterial electromagnetic cloak at microwave frequencies. *Science* **314**, 977–980 (2006).
12. W. Cai, U. K. Chettiar, A. V. Kildishev, V. M. Shalaev, Optical cloaking with metamaterials. *Nat. Photonics* **1**, 224–227 (2007).
13. G. W. Milton, J. R. Willis, On modifications of Newton's second law and linear continuum elastodynamics. *Proc. Phys. Soc. A* **463**, 855–880 (2007).
14. J. Mei, G. Ma, M. Yang, J. Yang, P. Sheng, *Acoustic Metamaterials and Phononic Crystals* (Springer, New York, 2013), pp. 159–199.
15. S. Yao, X. Zhou, G. Hu, Experimental study on negative effective mass in a 1D mass–spring system. *New J. Phys.* **10**, 043020 (2008).
16. Z. Liu, X. Zhang, Y. Mao, Y. Y. Zhu, Z. Yang, C. T. Chan, P. Sheng, Locally resonant sonic materials. *Science* **289**, 1734–1736 (2000).
17. Z. Liu, C. T. Chan, P. Sheng, Analytic model of phononic crystals with local resonances. *Phys. Rev. B* **71**, 014103 (2005).
18. N. Fang, D. Xi, J. Xu, M. Ambati, W. Srituravanich, C. Sun, X. Zhang, Ultrasonic metamaterials with negative modulus. *Nat. Mater.* **5**, 452–456 (2006).
19. J. Li, C. T. Chan, Double-negative acoustic metamaterial. *Phys. Rev. E. Stat. Nonlin. Soft Matter Phys.* **70**, 055602 (2004).
20. Y. Lai, Y. Wu, P. Sheng, Z.-Q. Zhang, Hybrid elastic solids. *Nat. Mater.* **10**, 620–624 (2011).
21. Y. Wu, Y. Lai, Z.-Q. Zhang, Elastic metamaterials with simultaneously negative effective shear modulus and mass density. *Phys. Rev. Lett.* **107**, 105506 (2011).
22. M. Yang, G. Ma, Z. Yang, P. Sheng, Coupled membranes with doubly negative mass density and bulk modulus. *Phys. Rev. Lett.* **110**, 134301 (2013).
23. T. Brunet, A. Merlin, B. Mascaro, K. Zimny, J. Leng, O. Poncelet, C. Aristégui, O. Mondain-Monval, Soft 3D acoustic metamaterial with negative index. *Nat. Mater.* **14**, 384–388 (2015).
24. Y. Ding, Z. Liu, C. Qiu, J. Shi, Metamaterial with simultaneously negative bulk modulus and mass density. *Phys. Rev. Lett.* **99**, 093904 (2007).
25. J. Christensen, Z. Liang, M. Willatzen, Metadevices for the confinement of sound and broadband double-negativity behavior. *Phys. Rev. B* **88**, 100301(R) (2013).
26. L. Fok, X. Zhang, Negative acoustic index metamaterial. *Phys. Rev. B* **83**, 214304 (2011).
27. S. H. Lee, C. M. Park, Y. M. Seo, Z. G. Wang, C. K. Kim, Acoustic metamaterial with negative density. *Phys. Lett. A* **373**, 4464–4469 (2009).
28. S. H. Lee, C. M. Park, Y. M. Seo, Z. G. Wang, C. K. Kim, Acoustic metamaterial with negative modulus. *J. Phys. Condens. Matter* **21**, 175704 (2009).
29. S. H. Lee, C. M. Park, Y. M. Seo, Z. G. Wang, C. K. Kim, Composite acoustic medium with simultaneously negative density and modulus. *Phys. Rev. Lett.* **104**, 054301 (2010).
30. N. Kaina, F. Lemoult, M. Fink, G. Lerosey, Negative refractive index and acoustic superlens from multiple scattering in single negative metamaterials. *Nature* **525**, 77–81 (2015).
31. M. Yang, G. Ma, Y. Wu, Z. Yang, P. Sheng, Homogenization scheme for acoustic metamaterials. *Phys. Rev. B* **89**, 064309 (2014).
32. Y. Wu, Y. Lai, Z.-Q. Zhang, Effective medium theory for elastic metamaterials in two dimensions. *Phys. Rev. B* **76**, 205313 (2007).
33. J. Mei, Z. Liu, W. Wen, P. Sheng, Effective dynamic mass density of composites. *Phys. Rev. B* **76**, 134205 (2007).
34. X. Zhou, G. Hu, Analytic model of elastic metamaterials with local resonances. *Phys. Rev. B* **79**, 195109 (2009).
35. M. Ambati, N. Fang, C. Sun, X. Zhang, Surface resonant states and superlensing in acoustic metamaterials. *Phys. Rev. B* **75**, 195447 (2007).
36. Z. Yang, J. Mei, M. Yang, N. H. Chan, P. Sheng, Membrane-type acoustic metamaterial with negative dynamic mass. *Phys. Rev. Lett.* **101**, 204301 (2008).
37. J. J. Park, K. J. B. Lee, O. B. Wright, M. K. Jung, S. H. Lee, Giant acoustic concentration by extraordinary transmission in zero-mass metamaterials. *Phys. Rev. Lett.* **110**, 244302 (2013).
38. Y. Jing, J. Xu, N. X. Fang, Numerical study of a near-zero-index acoustic metamaterial. *Phys. Lett. A* **376**, 2834–2837 (2012).
39. R. Fleury, A. Alù, Extraordinary sound transmission through density-near-zero ultranarrow channels. *Phys. Rev. Lett.* **111**, 055501 (2013).
40. Z. Yang, H. M. Dai, N. H. Chan, G. C. Ma, P. Sheng, Acoustic metamaterial panels for sound attenuation in the 50–1000 Hz regime. *Appl. Phys. Lett.* **96**, 041906 (2010).
41. C. J. Naify, C.-M. Chang, G. McKnight, S. Nutt, Transmission loss and dynamic response of membrane-type locally resonant acoustic metamaterials. *J. Appl. Phys.* **108**, 114905 (2010).
42. C. J. Naify, C.-M. Chang, G. McKnight, F. Scheulen, S. Nutt, Membrane-type metamaterials: Transmission loss of multi-celled arrays. *J. Appl. Phys.* **109**, 104902 (2011).
43. C. J. Naify, C.-M. Chang, G. McKnight, S. Nutt, Transmission loss of membrane-type acoustic metamaterials with coaxial ring masses. *J. Appl. Phys.* **110**, 124903 (2011).
44. G. Ma, M. Yang, Z. Yang, P. Sheng, Low-frequency narrow-band acoustic filter with large orifice. *Appl. Phys. Lett.* **103**, 011903 (2013).
45. S. Yao, X. Zhou, G. Hu, Investigation of the negative-mass behaviors occurring below a cut-off frequency. *New J. Phys.* **12**, 103025 (2010).
46. J. Pierre, B. Dollet, V. Leroy, Resonant acoustic propagation and negative density in liquid foams. *Phys. Rev. Lett.* **112**, 148307 (2014).
47. F. Lemoult, M. Fink, G. Lerosey, Acoustic resonators for far-field control of sound on a subwavelength scale. *Phys. Rev. Lett.* **107**, 064301 (2011).
48. F. Lemoult, N. Kaina, M. Fink, G. Lerosey, Wave propagation control at the deep subwavelength scale in metamaterials. *Nat. Phys.* **9**, 55–60 (2013).
49. H. Jia, M. Ke, R. Hao, Y. Ye, F. Liu, Z. Liu, Subwavelength imaging by a simple planar acoustic superlens. *Appl. Phys. Lett.* **97**, 173507 (2010).
50. J. Zhu, J. Christensen, J. Jung, L. Martin-Moreno, X. Yin, L. Fok, X. Zhang, F. J. Garcia-Vidal, A holey-structured metamaterial for acoustic deep-subwavelength imaging. *Nat. Phys.* **7**, 52–55 (2011).
51. J. B. Pendry, Negative refraction makes a perfect lens. *Phys. Rev. Lett.* **85**, 3966–3969 (2000).
52. V. G. Veselago, The electrodynamics of substances with simultaneously negative values of ε and μ. *Sov. Phys. Uspekhi* **10**, 509–514 (1968).
53. S. Zhang, L. Yin, N. Fang, Focusing ultrasound with an acoustic metamaterial network. *Phys. Rev. Lett.* **102**, 194301 (2009).
54. C. M. Park, J. J. Park, S. H. Lee, Y. M. Seo, C. K. Kim, S. H. Lee, Amplification of acoustic evanescent waves using metamaterial slabs. *Phys. Rev. Lett.* **107**, 194301 (2011).
55. J. J. Park, C. M. Park, K. J. B. Lee, S. H. Lee, Acoustic superlens using membrane-based metamaterials. *Appl. Phys. Lett.* **106**, 051901 (2015).
56. V. A. Podolskiy, E. E. Narimanov, Near-sighted superlens. *Opt. Lett.* **30**, 75–77 (2005).
57. Z. Liu, S. Durant, H. Lee, Y. Pikus, N. Fang, Y. Xiong, C. Sun, X. Zhang, Far-field optical superlens. *Nano Lett.* **7**, 403–408 (2007).
58. X. Zhang, Z. Liu, Superlenses to overcome the diffraction limit. *Nat. Mater.* **7**, 435–441 (2008).
59. Z. Jacob, L. V. Alekseyev, E. Narimanov, Optical Hyperlens: Far-field imaging beyond the diffraction limit. *Opt. Express* **14**, 8247–8256 (2006).
60. J. Christensen, F. J. García de Abajo, Anisotropic metamaterials for full control of acoustic waves. *Phys. Rev. Lett.* **108**, 124301 (2012).
61. V. M. García-Chocano, J. Christensen, J. Sánchez-Dehesa, Negative refraction and energy funneling by hyperbolic materials: An experimental demonstration in acoustics. *Phys. Rev. Lett.* **112**, 144301 (2014).

62. C. Shen, Y. Xie, N. Sui, W. Wang, S. A. Cummer, Y. Jing, Broadband acoustic hyperbolic metamaterial. *Phys. Rev. Lett.* **115**, 254301 (2015).

63. J. Li, L. Fok, X. Yin, G. Bartal, X. Zhang, Experimental demonstration of an acoustic magnifying hyperlens. *Nat. Mater.* **8**, 931–934 (2009).

64. J. B. Pendry, D. Schurig, D. R. Smith, Controlling electromagnetic fields. *Science* **312**, 1780–1782 (2006).

65. U. Leonhardt, Optical conformal mapping. *Science* **312**, 1777–1780 (2006).

66. H. Chen, C. T. Chan, P. Sheng, Transformation optics and metamaterials. *Nat. Mater.* **9**, 387–396 (2010).

67. L. Xu, H. Chen, Conformal transformation optics. *Nat. Photonics* **9**, 15–23 (2015).

68. H. Chen, C. T. Chan, Acoustic cloaking and transformation acoustics. *J. Phys. D Appl. Phys.* **43**, 113001 (2010).

69. A. N. Norris, Acoustic cloaking. *Acoust. Today* **11**, 38–46 (2015).

70. S. A. Cummer, D. Schurig, One path to acoustic cloaking. *New J. Phys.* **9**, 45 (2007).

71. H. Chen, C. T. Chan, Acoustic cloaking in three dimensions using acoustic metamaterials. *Appl. Phys. Lett.* **91**, 183518 (2007).

72. D. Torrent, J. Sánchez-Dehesa, Acoustic cloaking in two dimensions: A feasible approach. *New J. Phys.* **10**, 063015 (2008).

73. G. W. Milton, M. Briane, J. R. Willis, On cloaking for elasticity and physical equations with a transformation invariant form. *New J. Phys.* **8**, 248 (2006).

74. S. Zhang, C. Xia, N. Fang, Broadband acoustic cloak for ultrasound waves. *Phys. Rev. Lett.* **106**, 024301 (2011).

75. J. Li, J. B. Pendry, Hiding under the carpet: A new strategy for cloaking. *Phys. Rev. Lett.* **101**, 203901 (2008).

76. B.-I. Popa, L. Zigoneanu, S. A. Cummer, Experimental acoustic ground cloak in air. *Phys. Rev. Lett.* **106**, 253901 (2011).

77. L. Zigoneanu, B.-I. Popa, S. A. Cummer, Three-dimensional broadband omnidirectional acoustic ground cloak. *Nat. Mater.* **13**, 352–355 (2014).

78. W. Kan, B. Liang, X. Zhu, R. Li, X. Zou, H. Wu, J. Yang, J. Cheng, Acoustic illusion near boundaries of arbitrary curved geometry. *Sci. Rep.* **3**, 1427 (2013).

79. W. Kan, V. M. García-Chocano, F. Cervera, B. Liang, X.-Y. Zou, L.-L. Yin, J. Cheng, J. Sánchez-Dehesa, Broadband acoustic cloaking within an arbitrary hard cavity. *Phys. Rev. Appl.* **3**, 064019 (2015).

80. V. M. García-Chocano, L. Sanchis, A. Díaz-Rubio, J. Martínez-Pastor, F. Cervera, R. Llopis-Pontiveros, J. Sánchez-Dehesa, Acoustic cloak for airborne sound by inverse design. *Appl. Phys. Lett.* **99**, 074102 (2011).

81. M. D. Guild, A. Alù, M. R. Haberman, Cancellation of acoustic scattering from an elastic sphere. *J. Acoust. Soc. Am.* **129**, 1355–1365 (2011).

82. L. Sanchis, V. M. García-Chocano, R. Llopis-Pontiveros, A. Climente, J. Martínez-Pastor, F. Cervera, J. Sánchez-Dehesa, Three-dimensional axisymmetric cloak based on the cancellation of acoustic scattering from a sphere. *Phys. Rev. Lett.* **110**, 124301 (2013).

83. C. A. Rohde, T. P. Martin, M. D. Guild, C. N. Layman, C. J. Naify, M. Nicholas, A. L. Thangawng, D. C. Calvo, G. J. Orris, Experimental demonstration of underwater acoustic scattering cancellation. *Sci. Rep.* **5**, 13175 (2015).

84. Z. Liang, J. Li, Extreme acoustic metamaterial by coiling up space. *Phys. Rev. Lett.* **108**, 114301 (2012).

85. Y. Li, B. Liang, Z.-M. Gu, X.-Y. Zou, J.-C. Cheng, Unidirectional acoustic transmission through a prism with near-zero refractive index. *Appl. Phys. Lett.* **103**, 053505 (2013).

86. V. C. Nguyen, L. Chen, K. Halterman, Total transmission and total reflection by zero index metamaterials with defects. *Phys. Rev. Lett.* **105**, 233908 (2010).

87. Y. Wu, J. Li, Total reflection and cloaking by zero index metamaterials loaded with rectangular dielectric defects. *Appl. Phys. Lett.* **102**, 183105 (2013).

88. Q. Wei, Y. Cheng, X.-J. Liu, Acoustic total transmission and total reflection in zero-index metamaterials with defects. *Appl. Phys. Lett.* **102**, 174104 (2013).

89. F. Liu, Z. Liu, Elastic waves scattering without conversion in metamaterials with simultaneous zero indices for longitudinal and transverse waves. *Phys. Rev. Lett.* **115**, 175502 (2015).

90. R.-Q. Li, X.-F. Zhu, B. Liang, Y. Li, X.-Y. Zou, J.-C. Cheng, A broadband acoustic omnidirectional absorber comprising positive-index materials. *Appl. Phys. Lett.* **99**, 193507 (2011).

91. A. Climente, D. Torrent, J. Sánchez-Dehesa, Omnidirectional broadband acoustic absorber based on metamaterials. *Appl. Phys. Lett.* **100**, 144103 (2012).

92. C. J. Naify, T. P. Martin, C. N. Layman, M. Nicholas, A. L. Thangawng, D. C. Calvo, G. J. Orris, Underwater acoustic omnidirectional absorber. *Appl. Phys. Lett.* **104**, 073505 (2014).

93. X. Jiang, B. Liang, X.-Y. Zou, L.-L. Yin, J.-C. Cheng, Broadband field rotator based on acoustic metamaterials. *Appl. Phys. Lett.* **104**, 083510 (2014).

94. X. Jiang, L. Zhang, B. Liang, X.-Y. Zou, J.-C. Cheng, Radiation directivity rotation by acoustic metamaterials. *Appl. Phys. Lett.* **107**, 093506 (2015).

95. C. Shen, J. Xu, N. X. Fang, Y. Jing, Anisotropic complementary acoustic metamaterial for canceling out aberrating layers. *Phys. Rev. X* **4**, 041033 (2014).

96. C. Ren, Z. Xiang, Z. Cen, Design of acoustic devices with isotropic material via conformal transformation. *Appl. Phys. Lett.* **97**, 044101 (2010).

97. P. W. Klipsch, A low frequency horn of small dimensions. *J. Acoust. Soc. Am.* **13**, 137–144 (1941).

98. Z. Liang, T. Feng, S. Lok, F. Liu, K. B. Ng, C. H. Chan, J. Wang, S. Han, S. Lee, J. Li, Space-coiling metamaterials with double negativity and conical dispersion. *Sci. Rep.* **3**, 1614 (2013).

99. Y. Xie, B.-I. Popa, L. Zigoneanu, S. A. Cummer, Measurement of a broadband negative index with space-coiling acoustic metamaterials. *Phys. Rev. Lett.* **110**, 175501 (2013).

100. T. Frenzel, J. D. Brehm, T. Bückmann, R. Schittny, M. Kadic, M. Wegener, Three-dimensional labyrinthine acoustic metamaterials. *Appl. Phys. Lett.* **103**, 061907 (2013).

101. Y. Li, B. Liang, X. Tao, X.-F. Zhu, X.-Y. Zou, J.-C. Cheng, Acoustic focusing by coiling up space. *Appl. Phys. Lett.* **101**, 233508 (2012).

102. Y. Li, G. Yu, B. Liang, X. Zou, G. Li, S. Cheng, J. Cheng, Three-dimensional ultrathin planar lenses by acoustic metamaterials. *Sci. Rep.* **4**, 6830 (2014).

103. M. Molerón, M. Serra-Garcia, C. Daraio, Acoustic Fresnel lenses with extraordinary transmission. *Appl. Phys. Lett.* **105**, 114109 (2014).

104. K. Tang, C. Qiu, J. Lu, M. Ke, Z. Liu, Focusing and directional beaming effects of airborne sound through a planar lens with zigzag slits. *J. Appl. Phys.* **117**, 024503 (2015).

105. Y. Li, B. Liang, X.-Y. Zou, J.-C. Cheng, Extraordinary acoustic transmission through ultrathin acoustic metamaterials by coiling up space. *Appl. Phys. Lett.* **103**, 063509 (2013).

106. X. Cai, Q. Guo, G. Hu, J. Yang, Ultrathin low-frequency sound absorbing panels based on coplanar spiral tubes or coplanar Helmholtz resonators. *Appl. Phys. Lett.* **105**, 121901 (2014).

107. Y. Cheng, C. Zhou, B. G. Yuan, D. J. Wu, Q. Wei, X. J. Liu, Ultra-sparse metasurface for high reflection of low-frequency sound based on artificial mie resonances. *Nat. Mater.* **14**, 1013–1019 (2015).

108. Y. Li, B. Liang, Z.-M. Gu, X.-Y. Zou, J.-C. Cheng, Reflected wavefront manipulation based on ultrathin planar acoustic metasurfaces. *Sci. Rep.* **3**, 2546 (2013).

109. Y. Li, X. Jiang, R.-Q. Li, B. Liang, X.-Y. Zou, L.-L. Yin, J.-C. Cheng, Experimental realization of full control of reflected waves with subwavelength acoustic metasurfaces. *Phys. Rev. Appl.* **2**, 064002 (2014).

110. J. Mei, Y. Wu, Controllable transmission and total reflection through an impedance-matched acoustic metasurface. *New J. Phys.* **16**, 123007 (2014).

111. P. Peng, B. Xiao, Y. Wu, Flat acoustic lens by acoustic grating with curled slits. *Phys. Lett. A* **378**, 3389–3392 (2014).

112. Y. Xie, A. Konneker, B.-I. Popa, S. A. Cummer, Tapered labyrinthine acoustic metamaterials for broadband impedance matching. *Appl. Phys. Lett.* **103**, 201906 (2013).

113. Y. Xie, W. Wang, H. Chen, A. Konneker, B.-I. Popa, S. A. Cummer, Wavefront modulation and subwavelength diffractive acoustics with an acoustic metasurface. *Nat. Commun.* **5**, 5553 (2014).

114. W. Wang, Y. Xie, A. Konneker, B.-I. Popa, S. A. Cummer, Design and demonstration of broadband thin planar diffractive acoustic lenses. *Appl. Phys. Lett.* **105**, 101904 (2014).

115. K. Tang, C. Qiu, M. Ke, J. Lu, Y. Ye, Z. Liu, Anomalous refraction of airborne sound through ultrathin metasurfaces. *Sci. Rep.* **4**, 6517 (2014).

116. Y. Li, X. Jiang, B. Liang, J.-C. Cheng, L. Zhang, Metascreen-based acoustic passive phased array. *Phys. Rev. Appl.* **4**, 024003 (2015).

117. J. P. Arenas, M. J. Crocker, Recent trends in porous sound-absorbing materials. *J. Sound Vib.* **44**, 12–17 (2010).

118. D.-Y. Maa, Potential of microperforated panel absorber. *J. Acoust. Soc. Am.* **104**, 2861–2866 (1998).

119. J. Mei, G. Ma, M. Yang, Z. Yang, W. Wen, P. Sheng, Dark acoustic metamaterials as super absorbers for low-frequency sound. *Nat. Commun.* **3**, 756 (2012).

120. G. Ma, M. Yang, S. Xiao, Z. Yang, P. Sheng, Acoustic metasurface with hybrid resonances. *Nat. Mater.* **13**, 873–878 (2014).

121. X. Jiang, B. Liang, R.-Q. Li, X.-Y. Zou, L.-L. Yin, J.-C. Cheng, Ultra-broadband absorption by acoustic metamaterials. *Appl. Phys. Lett.* **105**, 243505 (2014).

122. P. Wei, C. Croënne, S. T. Chu, J. Li, Symmetrical and anti-symmetrical coherent perfect absorption for acoustic waves. *Appl. Phys. Lett.* **104**, 121902 (2014).

123. J. Z. Song, P. Bai, Z. H. Hang, Y. Lai, Acoustic coherent perfect absorbers. *New J. Phys.* **16**, 033026 (2014).

124. Y. Duan, J. Luo, G. Wang, Z. H. Hang, B. Hou, J. Li, P. Sheng, Y. Lai, Theoretical requirements for broadband perfect absorption of acoustic waves by ultra-thin elastic meta-films. *Sci. Rep.* **5**, 12139 (2015).

125. V. Leroy, A. Strybulevych, M. Lanoy, F. Lemoult, A. Tourin, J. H. Page, Superabsorption of acoustic waves with bubble metascreens. *Phys. Rev. B* **91**, 020301 (2015).

126. J. R. Piper, V. Liu, S. Fan, Total absorption by degenerate critical coupling. *Appl. Phys. Lett.* **104**, 251110 (2014).

127. M. Yang, C. Meng, C. Fu, Y. Li, Z. Yang, P. Sheng, Subwavelength total acoustic absorption with degenerate resonators. *Appl. Phys. Lett.* **107**, 104104 (2015).

128. A. Spadoni, C. Daraio, Generation and control of sound bullets with a nonlinear acoustic lens. *Proc. Natl. Acad. Sci. U.S.A.* **107**, 7230–7234 (2010).

129. F. Li, P. Anzel, J. Yang, P. G. Kevrekidis, C. Daraio, Granular acoustic switches and logic elements. *Nat. Commun.* **5**, 5311 (2014).

130. J. Lydon, M. Serra-Garcia, C. Daraio, Local to extended transitions of resonant defect modes. *Phys. Rev. Lett.* **113**, 185503 (2014).

131. P. Wang, F. Casadei, S. Shan, J. C. Weaver, K. Bertoldi, Harnessing buckling to design tunable locally resonant acoustic metamaterials. *Phys. Rev. Lett.* **113**, 014301 (2014).

132. B. Florijn, C. Coulais, M. van Hecke, Programmable mechanical metamaterials. *Phys. Rev. Lett.* **113**, 175503 (2014).

133. B.-I. Popa, S. A. Cummer, Nonreciprocal active metamaterials. *Phys. Rev. B* **85**, 205101 (2012).

134. B.-I. Popa, L. Zigoneanu, S. A. Cummer, Tunable active acoustic metamaterials. *Phys. Rev. B* **88**, 024303 (2013).

135. L. Airoldi, M. Ruzzene, Design of tunable acoustic metamaterials through periodic arrays of resonant shunted piezos. *New J. Phys.* **13**, 113010 (2011).

136. F. Casadei, T. Delpero, A. Bergamini, P. Ermanni, M. Ruzzene, Piezoelectric resonator arrays for tunable acoustic waveguides and metamaterials. *J. Appl. Phys.* **112**, 064902 (2012).

137. B.-I. Popa, S. A. Cummer, Non-reciprocal and highly nonlinear active acoustic metamaterials. *Nat. Commun.* **5**, 3398 (2014).

138. S. Xiao, G. Ma, Y. Li, Z. Yang, P. Sheng, Active control of membrane-type acoustic metamaterial by electric field. *Appl. Phys. Lett.* **106**, 091904 (2015).

139. R. Fleury, D. Sounas, A. Alù, An invisible acoustic sensor based on parity-time symmetry. *Nat. Commun.* **6**, 5905 (2015).

140. A. A. Maznev, A. G. Every, O. B. Wright, Reciprocity in reflection and transmission: What is a 'phonon diode'? *Wave Motion* **50**, 776–784 (2013).

141. D. Jalas, A. Petrov, M. Eich, W. Freude, S. Fan, Z. Yu, R. Baets, M. Popović, A. Melloni, J. D. Joannopoulos, M. Vanwolleghem, C. R. Doerr, H. Renner, What is—and what is not—an optical isolator. *Nat. Photonics* **7**, 579–582 (2013).

142. P. Roux, J. de Rosny, M. Tanter, M. Fink, The Aharonov-Bohm effect revisited by an acoustic time-reversal mirror. *Phys. Rev. Lett.* **79**, 3170 (1997).

143. R. Fleury, D. L. Sounas, C. F. Sieck, M. R. Haberman, A. Alù, Sound isolation and giant linear nonreciprocity in a compact acoustic circulator. *Science* **343**, 516–519 (2014).

144. B. Liang, X. S. Guo, J. Tu, D. Zhang, J. C. Cheng, An acoustic rectifier. *Nat. Mater.* **9**, 989–992 (2010).

145. B. Liang, B. Yuan, J.-C. Cheng, Acoustic diode: Rectification of acoustic energy flux in one-dimensional systems. *Phys. Rev. Lett.* **103**, 104301 (2009).

146. N. Boechler, G. Theocharis, C. Daraio, Bifurcation-based acoustic switching and rectification. *Nat. Mater.* **10**, 665–668 (2011).

147. Q. Wang, Y. Yang, X. Ni, Y.-L. Xu, X.-C. Sun, Z.-G. Chen, L. Feng, X.-P. Liu, M.-H. Lu, Y.-F. Chen, Acoustic asymmetric transmission based on time-dependent dynamical scattering. *Sci. Rep.* **5**, 10880 (2015).

148. M. Oudich, Y. Li, B. M. Assouar, Z. Hou, A sonic band gap based on the locally resonant phononic plates with stubs. *New J. Phys.* **12**, 083049 (2010).

149. M. Oudich, M. Senesi, M. B. Assouar, M. Ruzenne, J.-H. Sun, B. Vincent, Z. Hou, T.-T. Wu, Experimental evidence of locally resonant sonic band gap in two-dimensional phononic stubbed plates. *Phys. Rev. B* **84**, 165136 (2011).

150. M. Rupin, F. Lemoult, G. Lerosey, P. Roux, Experimental demonstration of ordered and disordered multiresonant metamaterials for lamb waves. *Phys. Rev. Lett.* **112**, 234301 (2014).

151. R. Zhu, X. N. Liu, G. L. Huang, H. H. Huang, C. T. Sun, Microstructural design and experimental validation of elastic metamaterial plates with anisotropic mass density. *Phys. Rev. B* **86**, 144307 (2012).

152. M. Farhat, S. Guenneau, S. Enoch, Ultrabroadband elastic cloaking in thin plates. *Phys. Rev. Lett.* **103**, 024301 (2009).

153. M. Farhat, S. Guenneau, S. Enoch, A. B. Movchan, Cloaking bending waves propagating in thin elastic plates. *Phys. Rev. B* **79**, 033102 (2009).

154. N. Stenger, M. Wilhelm, M. Wegener, Experiments on elastic cloaking in thin plates. *Phys. Rev. Lett.* **108**, 014301 (2012).

155. A. Colombi, P. Roux, S. Guenneau, M. Rupin, Directional cloaking of flexural waves in a plate with a locally resonant metamaterial. *J. Acoust. Soc. Am.* **137**, 1783–1789 (2015).

156. R. Zhu, X. N. Liu, G. K. Hu, C. T. Sun, G. L. Huang, Negative refraction of elastic waves at the deep-subwavelength scale in a single-phase metamaterial. *Nat. Commun.* **5**, 5510 (2014).

157. M. Dubois, M. Farhat, E. Bossy, S. Enoch, S. Guenneau, P. Sebbah, Flat lens for pulse focusing of elastic waves in thin plates. *Appl. Phys. Lett.* **103**, 071915 (2013).

158. M. Dubois, E. Bossy, S. Enoch, S. Guenneau, G. Lerosey, P. Sebbah, Time-driven super-oscillations with negative refraction. *Phys. Rev. Lett.* **114**, 013902 (2015)

159. M. Rupin, S. Catheline, P. Roux, Super-resolution experiments on lamb waves using a single emitter. *Appl. Phys. Lett.* **106**, 024103 (2015).

160. S. Brûlé, E. H. Javelaud, S. Enoch, S. Guenneau, Experiments on seismic metamaterials: Molding surface waves. *Phys. Rev. Lett.* **112**, 133901 (2014).

161. G. W. Milton, A. V. Cherkaev, Which elasticity tensors are realizable? *J. Eng. Mater. Technol.* **117**, 483–493 (1995).

162. G. W. Milton, *The Theory of Composites* (Cambridge Univ. Press, Cambridge, 2002).

163. M. Kadic, T. Bückmann, N. Stenger, M. Thiel, M. Wegener, On the practicability of penta-mode mechanical metamaterials. *Appl. Phys. Lett.* **100**, 191901 (2012).

164. T. Bückmann, N. Stenger, M. Kadic, J. Kaschke, A. Frölich, T. Kennerknecht, C. Eberl, M. Thiel, M. Wegener, Tailored 3D mechanical metamaterials made by dip-in direct-laser-writing optical lithography. *Adv. Mater.* **24**, 2710–2714 (2012).

165. X. Zheng, H. Lee, T. H. Weisgraber, M. Shusteff, J. DeOtte, E. B. Duoss, J. D. Kuntz, M. M. Biener, Q. Ge, J. A. Jackson, S. O. Kucheyev, N. X. Fang, Ultralight, ultrastiff mechanical metamaterials. *Science* **344**, 1373–1377 (2014).

166. T. Bückmann, M. Thiel, M. Kadic, R. Schittny, M. Wegener, An elasto-mechanical unfeel-ability cloak made of pentamode metamaterials. *Nat. Commun.* **5**, 4130 (2014).

167. Y. Li, Y. Wu, J. Mei, Double Dirac cones in phononic crystals. *Appl. Phys. Lett.* **105**, 014107 (2014).

168. J. Mei, Y. Wu, C. T. Chan, Z.-Q. Zhang, First-principles study of Dirac and Dirac-like cones in phononic and photonic crystals. *Phys. Rev. B* **86**, 035141 (2012).

169. F. Liu, X. Huang, C. T. Chan, Dirac cones at k = 0 in acoustic crystals and zero refractive index acoustic materials. *Appl. Phys. Lett.* **100**, 071911 (2012).

170. D. Torrent, D. Mayou, J. Sánchez-Dehesa, Elastic analog of graphene: Dirac cones and edge states for flexural waves in thin plates. *Phys. Rev. B* **87**, 115143 (2013).

171. D. Torrent, J. Sánchez-Dehesa, Acoustic analogue of graphene: Observation of Dirac cones in acoustic surface waves. *Phys. Rev. Lett.* **108**, 174301 (2012).

172. X. Huang, Y. Lai, Z. H. Hang, H. Zheng, C. T. Chan, Dirac cones induced by accidental degeneracy in photonic crystals and zero-refractive-index materials. *Nat. Mater.* **10**, 582–586 (2011).

173. M. Xiao, G. Ma, Z. Yang, P. Sheng, Z. Q. Zhang, C. T. Chan, Geometric phase and band inversion in periodic acoustic systems. *Nat. Phys.* **11**, 240–244 (2015).

174. L. Lu, J. D. Joannopoulos, M. Soljačić, Topological photonics. *Nat. Photonics* **8**, 821–829 (2014).

175. Z. Yang, F. Gao, X. Shi, X. Lin, Z. Gao, Y. Chong, B. Zhang, Topological acoustics. *Phys. Rev. Lett.* **114**, 114301 (2015).

176. X. Ni, C. He, X.-C. Sun, X.-P. Liu, M.-H. Lu, L. Feng, Y.-F. Chen, Topologically protected one-way edge mode in networks of acoustic resonators with circulating air flow. *New J. Phys.* **17**, 053016 (2015).

177. V. Peano, C. Brendel, M. Schmidt, F. Marquardt, Topological phases of sound and light. *Phys. Rev. X* **5**, 031011 (2015).

178. A. B. Khanikaev, R. Fleury, S. H. Mousavi, A. Alù, Topologically robust sound propagation in an angular-momentum-biased graphene-like resonator lattice. *Nat. Commun.* **6**, 8260 (2015).

179. M. Xiao, W.-J. Chen, W.-Y. He, C. T. Chan, Synthetic gauge flux and Weyl points in acoustic systems. *Nat. Phys.* **11**, 920–924 (2015).

180. P. Wang, L. Lu, K. Bertoldi, Topological phononic crystals with one-way elastic edge waves. *Phys. Rev. Lett.* **115**, 104302 (2015).

181. S. H. Mousavi, A. B. Khanikaev, Z. Wang, Topologically protected elastic waves in phononic metamaterials. *Nat. Commun.* **6**, 8682 (2015).

182. R. Süsstrunk, S. D. Huber, Observation of phononic helical edge states in a mechanical topological insulator. *Science* **349**, 47–50 (2015).

183. L. M. Nash, D. Kleckner, A. Read, V. Vitelli, A. M. Turner, W. T. M. Irvine, Topological mechanics of gyroscopic metamaterials. *Proc. Natl. Acad. Sci. U.S.A.* **24**, 14495–14500 (2015).

184. L. Lu, Z. Wang, D. Ye, L. Ran, L. Fu, J. D. Joannopoulos, M. Soljačić, Experimental observation of Weyl points. *Science* **349**, 622–624 (2015).

185. C. M. Bender, Making sense of non-Hermitian Hamiltonians. *Rep. Prog. Phys.* **70**, 947–1018 (2007).

186. W. D. Heiss, The physics of exceptional points. *J. Phys. Math. Theor.* **45**, 444016 (2012).

187. L. Feng, Y.-L. Xu, W. S. Fegadolli, M.-H. Lu, J. E. B. Oliveira, V. R. Almeida, Y.-F. Chen, A. Scherer, Experimental demonstration of a unidirectional reflectionless parity-time metamaterial at optical frequencies. *Nat. Mater.* **12**, 108–113 (2013).

188. L. Feng, Z. J. Wong, R.-M. Ma, Y. Wang, X. Zhang, Single-mode laser by parity-time symmetry breaking. *Science* **346**, 972–975 (2014).

189. B. Peng, Ş. K. Özdemir, S. Rotter, H. Yilmaz, M. Liertzer, F. Monifi, C. M. Bender, F. Nori, L. Yang, Loss-induced suppression and revival of lasing. *Science* **346**, 328–332 (2014).

190. X. Zhu, H. Ramezani, C. Shi, J. Zhu, X. Zhang, PT-symmetric acoustics. *Phys. Rev. X* **4**, 031042 (2014).

191. K. Ding, G. Ma, M. Xiao, Z. Q. Zhang, C. T. Chan, The emergence, coalescence and topological properties of multiple exceptional points and their experimental realization. arXiv:1509.06886 (2015).

192. C. Della Giovampaola, N. Engheta, Digital metamaterials. *Nat. Mater.* **13**, 1115–1121 (2014).

193. Y. Xie, T.-H. Tsai, A. Konneker, B.-I. Popa, D. J. Brady, S. A. Cummer, Single-sensor multi-speaker listening with acoustic metamaterials. *Proc. Natl. Acad. Sci. U.S.A.* **112**, 10595–10598 (2015).

194. G. Ma, thesis, Hong Kong University of Science and Technology (2012).

Science Advances

Acoustic metamaterials: From local resonances to broad horizons

Guancong Ma and Ping Sheng (February 26, 2016)
Sci Adv 2016, 2:.
doi: 10.1126/sciadv.1501595

The following resources related to this article are available online at http://advances.sciencemag.org. (This information is current as of October 23, 2016):

Updated information and services, including high-resolution figures, can be found in the online version of this article at:
http://advances.sciencemag.org/content/2/2/e1501595.full

This article **cites 190 articles,** 14 of which you can access for free at:
http://advances.sciencemag.org/content/2/2/e1501595#BIBL